Nonlinear Dynamics (2026) 114:218
https://doi.org/10.1007/s11071-025-12088-x

RESEARCH

Numerical and experimental studies on a bistable oscillator coupled with a resonator for vibration attenuation and chaos prediction

Tugberk Guner[1] · Oreste S. Bursi[1] · Alessandro Marzani[2] · Antonio Palermo[2]

Received: 28 July 2025 / Revised: 19 October 2025 / Accepted: 25 November 2025

Abstract
In this study, we develop and investigate an analytical model of a bistable damped oscillator coupled with a linear resonator, supported by numerical simulations and experimental validation. Bistability is realised through slender beams buckled under axial compression, forming the core of the system. The proposed analytical and numerical tools can capture the key nonlinear dynamics of the coupled system. The response of the bistable oscillator–linear resonator system under external excitation is initially analysed and compared with that of a stand-alone oscillator. By varying excitation amplitude and frequency, a rich spectrum of nonlinear behaviours is revealed—from intrawell oscillations to interwell transitions and bifurcations—and is thoroughly characterised. The integration of a linear resonator is shown to enhance vibration attenuation across multiple frequency bands and improve the predictability of chaotic regimes. Experimental validation is then conducted using additively manufactured pre-buckled bistable beams and linear resonators. Nonlinear system identification confirms the influence of friction and complex damping, aligning well with predictions. Tests which compare oscillators with linear and bistable beams coupled to resonators demonstrate the effectiveness of pre-buckled beams in producing bistable springs. Finally, simulation accuracy is shown to degrade significantly close to chaotic response regimes, emphasising the sensitivity of bistable systems to parameter variations, test conditions, and manufacturing tolerances.

Keywords Bistable oscillator · Buckled beam · Chaotic dynamics · Experimental validation · Nonlinear system identification · Friction · High-order damping

1 Introduction

1.1 Background and motivation

Bistable mechanical systems, which feature two stable equilibrium states, exhibit various static and dynamic properties not found in monostable systems. Although bistability is the first step in multi-stable mechanics/dynamics [1], researchers have been challenged by its dynamics and regime variety. This has prompted them to investigate the discovery of these assets more deeply and to develop more intuitive and unique applications to solve real-world problems. In general, two stable equilibrium states are linked to different geometrical configurations, such as twisting or buckling, with a snap-through action between these states with negative stiffness behaviour. This leads to a decrease in the restoring forces, large displacements, accompanied by changes in curvature and strain. Consequently, these large displacements do not require a continuous input to sustain motion, as is the case in linear systems [2].

The uniqueness of bistable mechanisms has made them viable candidates for applications across various fields, including engineering, materials science, physics, and beyond [3]. Since these systems operate with low dynamic stiffness associated with large displacements, a large amount of energy can be absorbed, stored stably, and possibly reversed [4]. This unique property makes them ideal for applications that require energy absorption and dissipation against vibration and impact [5–9].

With recent advancements in piezoelectric materials, bistability has also found applications in energy harvesting [10, 11]. The large amplitude and velocity motions between

✉ Oreste S. Bursi
oreste.bursi@unitn.it

[1] Department of Civil, Environmental and Mechanical Engineering, University of Trento, Via Mesiano, 77, 38123 Trento, TN, Italy

[2] Department of Civil, Chemical, Environmental, and Materials Engineering, University of Bologna, Via Risorgimento, 2, 40136 Bologna, BO, Italy

Published online: 11 February 2026

stable states increased power generation [12]. Moreover, the harmonic diffusion property of bistability [2] represents a potential solution to vibration-based energy harvesting, where performance is limited to excitations close to the resonance frequency of the system [13]. Nonetheless, a significant disadvantage of the bistable systems adopted as energy harvesters is the potential presence of aperiodic or chaotic responses. This can lead to the need for complex circuits, thus reducing their performance [11]. The presence of snap-through dynamics may clearly lead to chaotic responses, which reveal underlying patterns and deterministic laws within the apparent randomness of chaos [14]. The butterfly effect [15], characterised by sensitivity to initial conditions, results in diverse and intricate dynamic response characteristics. Thus, to enhance the performance of bistable energy harvesters, active control strategies have been devised [16, 17].

Bistability has also been extensively used in acoustic and elastic metamaterials and metastructures, which may exhibit unusual properties due to wave manipulation [18]. In particular, these periodic or finite lattice systems can showcase distinctive properties such as tensegrity [19], chirality [20], deployability [21], auxeticity [22], self-locking [23], and foldability [24]. These and other applications led to the development of deployable air and space structures, which facilitate compact designs in the aerospace industry [25–27]. Bistability has also been utilised in nonlinear energy sinks (NES) [28]. Zeng et al. [29] demonstrated micro-amplitude vibration suppression using a bistable NES composed of buckled beams. Whilst the dynamics of periodic mechanical structures containing bistable elastic elements has been well understood [30], their advantages in the low-frequency regime and the presence of locally resonant components, i.e. resonators [31], have not yet been taken into account. See, in this respect, the analytical/numerical research work of Guner et al. [32] that, on a large scale, protected an industrial tank from strong earthquakes, with finite locally resonant metafoundations endowed with bistable buckled columns.

Recent advances in additive manufacturing (AM) techniques have enabled faster and more efficient production of mock-ups for experimental validation [33, 34]. Among these techniques, fused deposition modelling (FDM) has gained popularity due to its accessibility and affordability. FDM has been particularly useful for fabricating bistable systems, which often demand complex geometries and directional flexibility [35–37]. However, whilst AM facilitates the creation of such intricate designs, the accurate characterisation of these systems remains challenging due to their inherent nonlinear behaviour.

In particular, the identification of mechanical properties in metamaterials and metastructures – especially those incorporating strong nonlinearity, e.g. bistability—poses significant difficulties. Several studies have addressed related challenges; for example, Chuang et al. [38] applied a method for beam crack detection, whilst Aloschi et al. [39] proposed a time-domain procedure to extract dispersion curves and mechanical properties, including damping, in linear and nonlinear one-dimensional periodic structures. Characterising mock-up systems that include bistability is even more complex, primarily due to nonlinear damping mechanisms often influenced by friction. Accurate identification of these damping parameters typically involves a large number of variables, leading to the well-known issue of non-uniqueness, especially when only limited response data are available [40].

1.2 Scope and core contribution

In sum, although many investigations have been carried out on bistable mechanical systems [3, 12], several aspects still need to be analysed in depth. In particular, we underline: (i) a bistable oscillator with the presence of a resonator that can clearly influence the dynamic response of the coupled system; (ii) the peculiarities related to the realisation of a bistable mock-up with buckling beams in view of physical testing; and (iii) the effects related to static/kinetic friction and high-order damping and its characterisation. The goal of this study is to establish a clear understanding of how a linear resonator modifies the nonlinear dynamics of a bistable oscillator. By combining analytical modelling, simulations, and experiments, the work aims to bridge the gap between theoretical predictability and experimental observability. Along these lines, a bistable damped oscillator coupled with a linear damped resonator is proposed and investigated by means of numerical and experimental approaches. The proposed systems are depicted in Fig. 1, where bistability is realised with slender beams buckled under axial compression.

Hence, the paper is organised as follows. Section 2 introduces the analytical formulation of a bistable oscillator with a local resonator and provides an analytical treatment useful to approximate its response. Extensive numerical analyses are instead conducted in Sect. 3 to investigate in depth the corresponding dynamics. More specifically, the influence of the main cell coupled with the resonator in different harmonic regimes, chaos, and vibration characteristics was studied. Section 4 provides the basis of the experimental campaign aimed at validating numerical results; test equipment and a bistable oscillator mock-up have been designed and, for comparison, linear oscillator prototypes have also been manufactured. The identification of relevant parameters has been conducted in Sect. 5; in particular, the results revealed the presence of significant nonlinear damping and friction that have been quantified and modelled. Consequently, the experimental results are presented in Sect. 6, discussed for vibration suppression and chaos prediction; also, comparisons between experiments and numerical results are carried out. Finally, Sect. 7 presents conclusions and describes future developments.

2 Modelling and analysis

A simple bistable oscillator subjected to a harmonic driven boundary input $x_0(t) = A_0 e^{i\omega_0 t}$ with amplitude A_0 and frequency ω_0, shown in Fig. 1c, can be represented as a second-order nonlinear differential equation,

$$m_m \ddot{x}_m + c_m \dot{x} - k_1 x + k_3 x^3 = 0 \tag{1}$$

where $x = x(t) = x_m(t) - x_0(t)$ represents the relative vertical displacement, k_1 and k_3 are positive spring constants, and dots represent the derivative with respect to time. It is noted that Eq. (1) assumes one-dimensional motion of the oscillator and limits the restoring force nonlinearity to a cubic term. These assumptions are standard for reduced-order bistable oscillator models and are adequate to capture the essential nonlinear dynamics observed in the experiments. The corresponding force of the bistable spring, $F = -k_1 x + k_3 x^3$ vs. displacement relationship and its potential energy, $V = -1/2 k_1 x^2 + 1/4 k_3 x^4$, are given in Fig. 2a, where two stable points, $x = \pm\delta_s = \pm\sqrt{k_1/k_3}$, and the unstable point at $x = 0$ are highlighted. The linearised stiffness values of the bistable system at these points read $dF(x = \pm\delta_s)/dx = 2k_1$ and $dF(x = 0)/dx = -k_1$, respectively. At the unstable point, $x = 0$, the system exhibits the peak negative stiffness. Evidently, both linearised stiffness terms are independent of the cubic stiffness term, k_3.

By replacing $\hat{x} = x/\delta_s$, $\tau = t\omega_n$, and $\omega_n = \sqrt{k_1/m_m}$, Eq. (1) is made non-dimensional and reads,

$$\hat{x}_m'' + \eta \hat{x}' - \hat{x} + \varepsilon \hat{x}^3 = 0 \tag{2}$$

where $\eta = c(m_m \omega_n)^{-1}$, $\varepsilon = k_3 \delta_s^2 \left(m_m \omega_n^2\right)^{-1}$, and $\hat{x}_0 = \alpha e^{i\Omega\tau}$ with $\Omega = \omega_0/\omega_n$ and $\alpha = A_0/\delta_s$ The occurrence of snap-through during the oscillations characterises the type of motion: intrawell, low amplitude interwell, high amplitude interwell motions, as exemplified in Fig. 2b, in which steady-state responses for varying input amplitudes are given. Furthermore, it is evident that interwell dynamics can exhibit not only multi-harmonic periodic behaviours but also transition from periodic interwell oscillations to quasi-periodic interwell oscillations—bifurcations -, including chaotic responses. [2, 28].

As anticipated in the Subsection Scope and inspired by locally resonant metastructures [32], we intend to study bistable oscillators coupled with linear resonators in depth. The proposed two-DoFs system is drafted in Fig. 1b, d, where the resonator with mass m_r is connected to the main mass with a linear spring and damper. The non-dimensional system of equations of motion (EoM) reads,

$$\hat{x}_m'' + \eta \hat{x}' - \hat{x} + \varepsilon \hat{x}^3 + \varphi \eta_r (\hat{x}_m' - \hat{x}_r') + \varphi \lambda^2 (\hat{x}_m - \hat{x}_r) = 0 \tag{3a}$$

$$\hat{x}_r'' + \eta_r (\hat{x}_r' - \hat{x}_m') + \lambda^2 (\hat{x}_r - \hat{x}_m) = 0 \tag{3b}$$

where $\eta_r = c_r (m_r \omega_n)^{-1}$, $\omega_r = \sqrt{k_r/m_r} = \lambda \omega_n$, and $m_r = m_m \varphi$.

Analytical solutions for the Duffing oscillators are available in the literature and are valid under the assumption of periodic response. However, as underlined in [11], the possibility of aperiodic responses limits the use of these solutions. In the case of the coupled oscillator, Fig. 1, as further demonstrated in Sect. 3, near the resonator's tuned frequency, periodic responses can be ensured. For brevity, herein, the response is assumed to be periodic, and an analytical solution is sought. Other cases are considered in Sect. 3. In addition, as the mock-up discussed in Sect. 4 is driven through a sinusoidal input, for consistency, subsequent analyses are carried out considering $\hat{x}_0(t) = \alpha sin(\Omega\tau)$. Consequently, Eq. (3) can be expressed as follows:

$$\begin{aligned} &\hat{x}_m'' + \eta(\hat{x}_m' - \alpha\Omega cos(\Omega\tau)) \\ &\quad - (\hat{x}_m - \alpha sin(\Omega\tau)) + \varepsilon(\hat{x}_m - \alpha sin(\Omega\tau))^3 \\ &\quad + \varphi\eta_r(\hat{x}_m' - \hat{x}_r') + \varphi\lambda^2(\hat{x}_m - \hat{x}_r) = 0 \end{aligned} \tag{4a}$$

$$\hat{x}_r'' + \eta_r(\hat{x}_r' - \hat{x}_m') + \lambda^2(\hat{x}_r - \hat{x}_m) = 0 \tag{4b}$$

Assuming a periodic response at steady-state, an analytical solution of (4) can be obtained by means of the Harmonic Balance Method (HBM) [41]. Accordingly, neglecting the third- and higher order harmonics, the ansatz follows:

$$\bar{x_m} = a_1 sin(\Omega\tau) + b_1 cos(\Omega\tau) \tag{5a}$$

$$\bar{x_r} = a_{r,1} sin(\Omega\tau) + b_{r,1} cos(\Omega\tau) \tag{5b}$$

then, We set $\bar{a}_1 = a_1 + \alpha$, and therefore, (4) can be written in terms of relative quantities, as:

$$\begin{aligned} &\hat{x}_m'' + \eta(\hat{x}_m') - (\hat{x}_m) + \varepsilon(\hat{x}_m)^3 + \varphi\eta_r(\hat{x}_m' - \hat{x}_r') \\ &\qquad + \varphi\lambda^2(\hat{x}_m - \hat{x}_r) \\ &\qquad = -\alpha\Omega^2 sin(\Omega\tau) \end{aligned} \tag{6a}$$

$$\hat{x}_r'' + \eta_r(\hat{x}_r' - \hat{x}_m') + \lambda^2(\hat{x}_r - \hat{x}_m) = -\varphi\alpha\Omega^2 sin(\Omega\tau) \tag{6b}$$

To avoid redundant solutions and increase stability, the Cartesian coordinates can be expressed in amplitude-phase form. Accordingly, the insertion of the ansatz in Eq. (6b), and the transformation to polar coordinates entails,

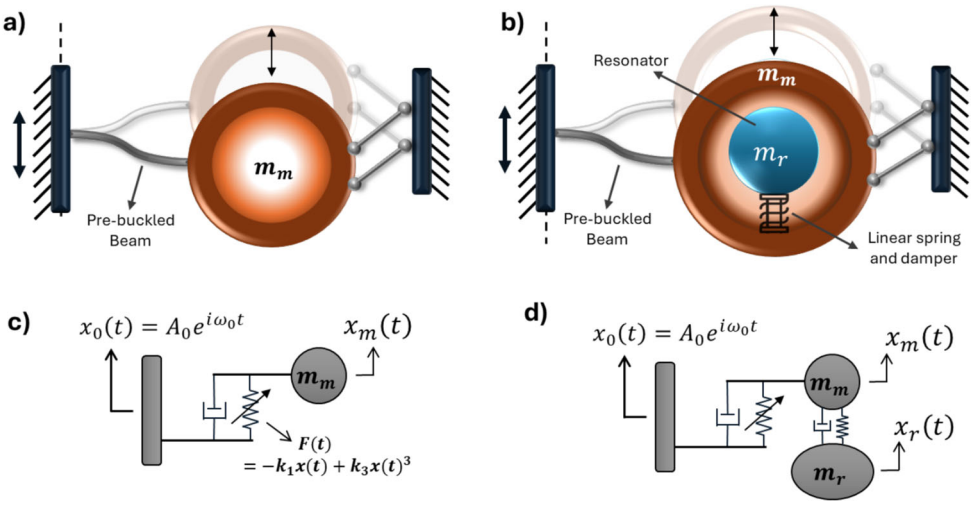

Fig. 1 Bistable oscillators subjected to a driven boundary excitation $x_0(t)$ and relative motion $x(t) = x_1(t) - x_0(t)$ **a** a bistable oscillator composed of pre-buckled beams and main mass; **b** a bistable oscillator coupled with a linear resonator; **c** mass-spring-damper model of the stand-alone bistable oscillator; **d** mass-spring-damper model of the bistable oscillator coupled with a linear resonator

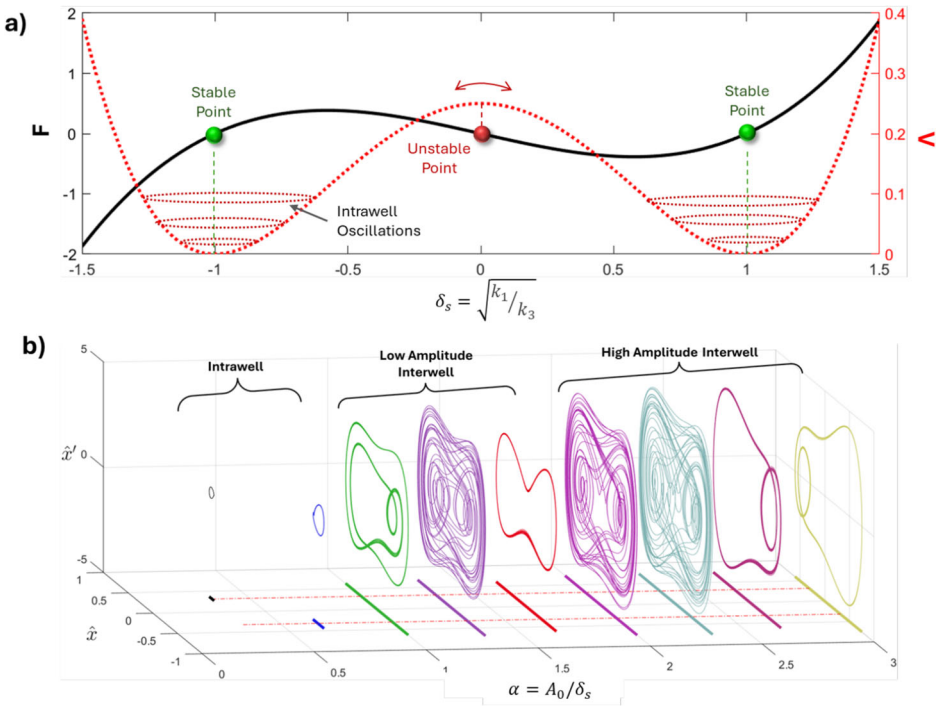

Fig. 2 Bistable Duffing oscillator response: **a** Force-displacement and potential energy relationships; **b** phase portraits for various steady-state responses ($\Omega = 0.5$)

$$a_{r,1} = \frac{\left(\lambda^2 - \Omega^2\right)\left(\lambda^2 q \sin(Q) - \alpha\varphi\omega^2\right) + (\eta_r\Omega)^2 q \sin(Q) + q\eta_r\Omega^3 \cos(Q)}{\left(\lambda^2 - \Omega^2\right)^2 + (\eta_r\Omega)^2} \tag{7a}$$

$$b_{r,1} = \frac{\left(\lambda^2(\lambda^2 - \Omega^2) + (\eta_r\Omega)^2\right) q \cos(Q) - q\eta_r\Omega^3 \sin(Q) + \alpha\eta_r\varphi\Omega^3}{\left(\lambda^2 - \Omega^2\right)^2 + (\eta_r\Omega)^2} \tag{7b}$$

in which $\bar{a}_1^2 + b_1^2 = (qsin(Q))^2 + (qcos(Q))^2 = q^2$. The insertion of (7a) in (6a), results in:

$$\begin{aligned}&\left(qf_1f_2\cos(Q) + q\left[f_3\cos(Q) + \Omega f_4\sin(Q)\right] - \alpha\eta_r\varphi\Omega^5\right)cos(\Omega\tau)\\&+\left(qf_1f_2\sin(Q) + q\left[f_3\sin(Q) - \Omega f_4\cos(Q)\right] + \alpha\eta_r^2\varphi\Omega^4\right.\\&\left.+\alpha\Omega^2\left[f_4 - (\lambda^2-\Omega^2)\varphi\lambda^2\right]\right)sin(\Omega\tau)\\&+[\cdots]cos(3\Omega\tau) + [\cdots]sin(3\Omega\tau) = 0\end{aligned} \tag{8}$$

where:

$$\begin{aligned}f_1 &= 3\varepsilon q^2/4 - 1\\f_2 &= (\lambda^2-\Omega^2)^2 + \eta_r^2\Omega^2\\f_3 &= (\lambda^2-\Omega^2)^3 - (\lambda^2-\Omega^2)\lambda^4 + 2\eta_r^2\lambda^2\Omega^2\\f_4 &= (\lambda^2-\Omega^2)^2(\eta+\eta_r) + \eta\eta_r^2\Omega^2 + (\lambda^2-\Omega^2)\eta_r\lambda^2\end{aligned}$$

Ignoring high-order harmonics, the balance of first-order harmonic terms entails,

$$\left(\frac{q}{\alpha\Omega^2}\right)^2 = \frac{(-\varphi\Omega^2(\eta_r^2+\lambda^2) + \lambda^4\varphi - f_4)^2 + (\eta_r\varphi\Omega^3)^2}{(f_3 + f_1 f_2)^2 + (f_4\Omega)^2} \tag{9}$$

Eq. (9) is numerically solved, and the comparative results for the stand-alone bistable oscillator with $\varepsilon = 1, \eta = 0.1$, and the coupled oscillator with the resonator endowed with $\eta_r = 1.5, \varphi = 2, and\, \lambda = 0.8$, are shown in Fig. 3a, b, respectively. In the absence of the resonator, multiple intrawell and interwell periodic motions can simultaneously exist above $\Omega = 0.5$, except for $\alpha = 2$, where periodic interwell are present and the response is always beyond $2\delta_s$ as understood from Fig. 2a.

The presence of the resonator prevents bifurcations around its tuned frequency range $\lambda = 0.8$, and except the case $\alpha = 2$, it prevents interwell motions. In particular, at $\alpha = 0.2$, interwell responses occur only up to $\Omega = 0.5$, and above, no periodic interwell response is found. For higher α values, interwell periodic motions can occur after resonator attenuation. At $\alpha = 2.0$ the coupled system exhibits a prominent single steady state with high interwell, except for low frequencies, where both low and high interwell periodic responses are possible.

3 Dynamics of a bistable oscillator coupled with a linear resonator

To shed further light on Fig. 3, herein the fundamental dynamics of the bistable oscillator also coupled with a linear resonator, including aperiodic responses, is analysed. In this respect, the explicit fourth-order Runge–Kutta method was used to integrate in time both (2) and the system of EoM (3). The validity of the numerical results was proved experimentally in Sect. 4.

3.1 Harmonic Diffusion, Chaos Spectra and Vibration Characteristics

Bifurcation diagrams that show the oscillators response $\hat{x}$ with $\hat{x}' = 0$) at various input amplitudes α around resonance, i.e. for $\Omega = 1$ and $\Omega = 1.2$ are provided in Fig. 4. For the case of $\Omega = 1$, i.e. $\omega_0 = \omega_n$, between $0 < \alpha < 1.9$ the increase in periodic response amplitude is evident. The presence of the resonator anticipated the interwell periodic regimes. Nevertheless, the presence of resonators increases bifurcations and aperiodic responses at high amplitude inputs; clearly, proper resonator tuning can entail high amplitude interwell motions, which is important for vibration mitigation and energy harvesting applications [12, 32].

In view of a better understanding of the complex dynamics of the coupled oscillator at hand, several tools were developed, which are presented in Fig. 5. In particular, the forced response of the oscillators permits quantification of the distribution of frequency peaks, i.e. the Harmonic Diffusion, either in the periodic or chaotic regimes. The regions of chaotic responses, instead, are quantified by means of the evaluation of Lyapunov exponents. In this respect, the largest Lyapunov exponent (LLE) technique had been adopted by means of the algorithm proposed by Rosenstein et al. [42]. Lastly, the frequency response function (FRF) was calculated:

$$FRF(\omega_0) = 20log_{10}\left(\frac{max|\dot{x}_{out}|}{max|\dot{x}_{in}|}\right) = 20log_{10}\left(\frac{max|\dot{x}|)}{A_0\omega_0}\right) \tag{10}$$

with reference to velocities that can be more easily estimated than displacements due to possible interwell motions. FRF is used to identify regions of amplification (FRF > 0) or attenuation (FRF < 0). For each simulation, the bistable oscillators were subjected to a range of amplitudes, i.e. $\alpha \leq 3$ and frequencies, i.e. $\Omega \leq 3$.

Along these lines, Fig. 6 presents the outcome of the Harmonic Diffusion analysis depicted in Fig. 5 for both the case without and with resonator; at $\alpha = 1/3$ and $\alpha = 3$. The dashed lines define the integer multiples (1,2,3,...) of the input frequency, Ω. Multiple points in a vertical line represent the well-known harmonic diffusion phenomenon and the diffusion of input energy to higher frequencies. In the case of no resonator, in the low input frequency range, the response is equivalent to the input frequency, whilst for $\Omega > 1.5$, multiple peaks are seen for $0.7 < \Omega_{peaks} < 2$. This specific response is characterised by aperiodicity and is highlighted by blue circles. The presence of a resonator clearly shifts the

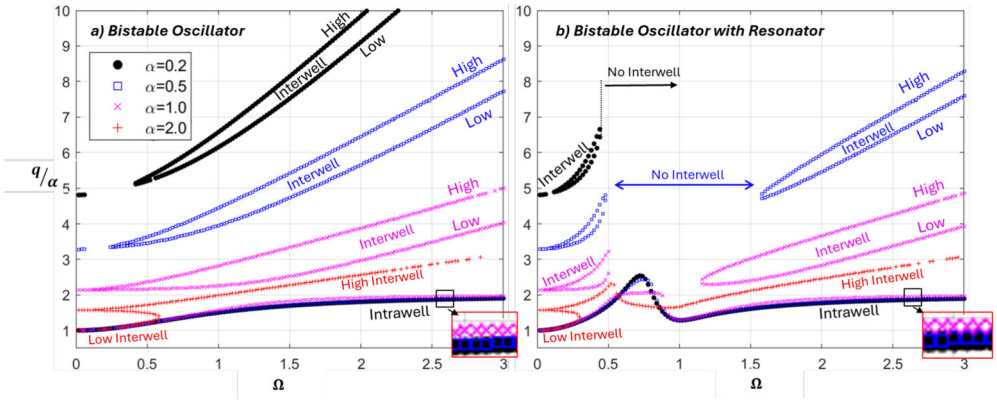

Fig. 3 Frequency response solutions obtained from (9): **a** Bistable oscillator ($\varepsilon = 1, \eta = 0.1$); **b** Bistable oscillator coupled with a linear resonator ($\eta_r = 1.5, \varphi = 2,\ and\ \lambda = 0.8$)

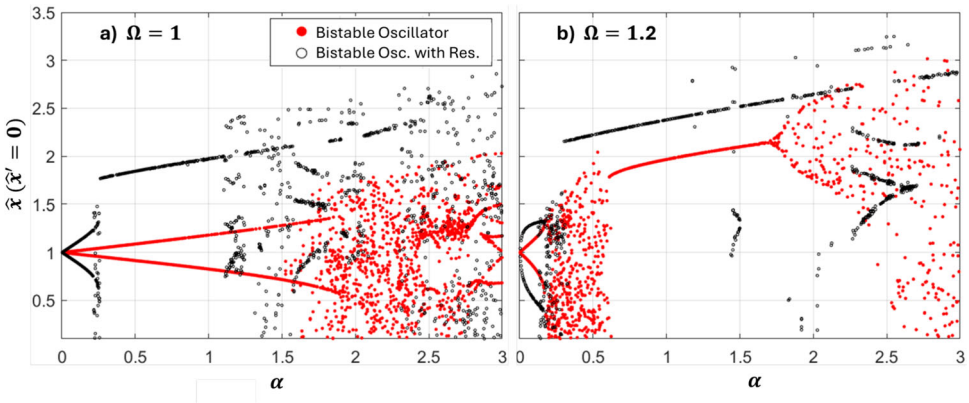

Fig. 4 Bifurcation diagrams comparing stand-alone bistable oscillator and the bistable oscillator with a resonator; **a** response for $\Omega = 1 (\omega_0 = \omega_n)$; **b** response for $\Omega = 1.2$ ($\varepsilon = 1, \eta = 0.1, \eta_r = 0.075, \varphi = 2$, and $\lambda = 0.8$)

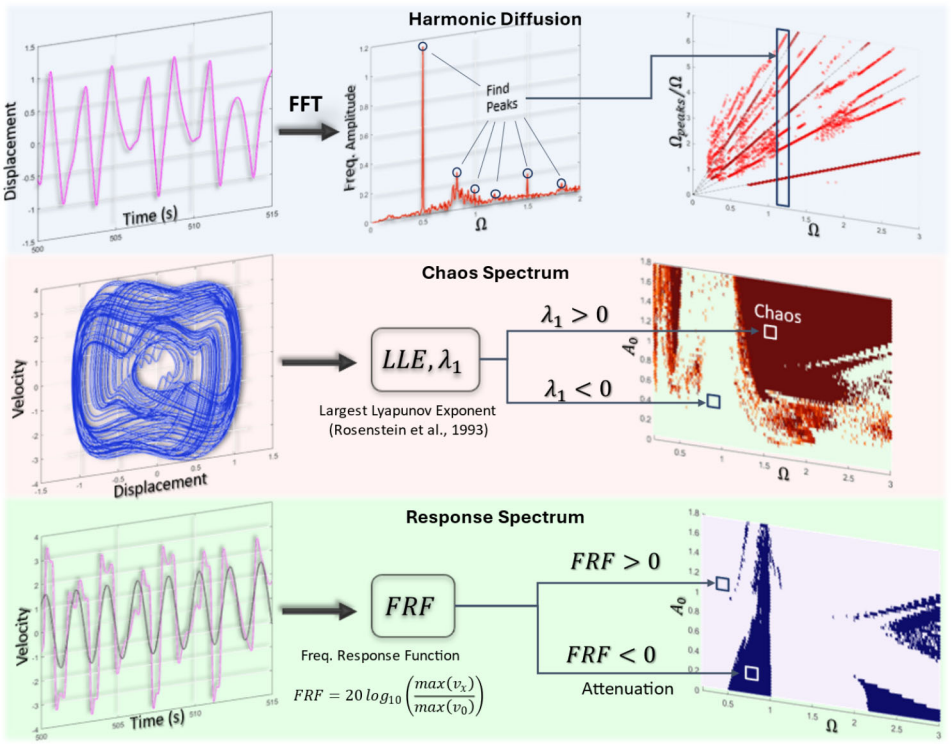

Fig. 5 Numerical tools adopted and typical outcomes to characterise the response of bistable oscillators

chaotic region to the low amplitude-low frequency region; more importantly, in the high frequency range, i.e. $\Omega > 1.7$, as a result of additional damping between the resonator and main mass, the Harmonic diffusion concentrates between the 1st and 3rd harmonics, exhibiting a periodic response, in agreement with the analytical solutions presented in Sect. 2.

For both the stand-alone bistable oscillator and the oscillator coupled with a resonator, the type of motion in the steady-state regime and the LLE values are depicted in Fig. 7. Within the intrawell regime, LLE values are negative, corresponding to a periodic response. Conversely, transition regimes between wells entail aperiodic responses or chaos. In addition, the bistable oscillator with a resonator, see Fig. 7d, entails a large region of periodic motion at lower input frequencies Ω.

In terms of vibration mitigation properties, understanding the relationship between response output and input is important. Therefore, $FRF(\omega_0)$ values were computed, where negative FRF values correspond to favourable response attenuation. Relevant results are shown in Fig. 8. The bistable oscillator exhibits response attenuation only at high frequency and low amplitude, whereas the presence of the resonator entails new attenuation regions both at its tuned frequency $\lambda = 0.8$ up to $\alpha = 1.5$ and around $\alpha = 1$ and $\Omega > 2$.

3.2 Parametric study

To quantify the effect of the other parameters involved, i.e. $\eta, \eta_r, \lambda, \varphi$ on the response of the bistable oscillator, the FRF and LLE values have been quantified. More specifically, the effect of the damping ratio η involved in Eq. (2) on the values of FRF and LLE is shown in Fig. 9. Increased damping ratios lead to more attenuation zones, particularly at higher frequencies. In addition, a favourable benefit is observed in terms of stable regions of response.

The presence of the resonator in the system of EoM (3), introduces three additional parameters, η_r, λ, φ to be taken into account. Their effects on FRF and LLE values are presented in Figs. 10, 11 and 12. In particular, Fig. 10a–c shows that the increase in η_r entails a new attenuation branch at the anti-resonance frequency and the high amplitude range *(10-I)*, whilst a transmission amplitude band appeared between $0.5 < \alpha < 1.0$. With regard to the LLE results, the increased resonator damping entails some chaotic regions around the attenuation frequency range *(10-II)*. Moreover, the increased damping value creates an attenuation zone at high frequency and amplitude ranges, see *(10-III)*, which results in less and weaker chaotic motions w.r.t. the case without resonator.

The effects of λ, with $\omega_r = \sqrt{k_r/m_r} = \lambda\omega_n$, i.e. of various stiffness values of the resonator, can be observed in Fig. 11. If one focusses on the resonator's tuned frequency range, at low amplitude, the attenuation zone is evident, as indicated in *(11-III)*. In the high-amplitude range, a couple of attenuation zones can be observed in the anti-resonance frequency range in *(11-I)*. Moreover, increased stiffness values result in more propagation in the high-frequency amplitude range, for $0.5 < \alpha < 1.0$, as observed in *(11-II)*. Similarly, at higher amplitude values, less chaotic responses are observed, as indicated in *(11-IV)*.

The cases corresponding to a few resonator mass ratios φ, are presented in Fig. 12. *(12-I)* shows a favourable increase in the attenuation zone, whilst the attenuation diminishes at high-amplitude values. With regard to LLE values, the stable zones increase both for higher amplitudes, see *(12-II)*, and frequency, as shown in *(12-III)*.

3.3 Energy dissipation characteristics

Given the high velocities $\hat{x}'_m$ and $\hat{x}'_r$ exhibited by the stand-alone bistable oscillator and with the resonator during the interwell motion, it is worthwhile to quantify the associated dissipated energies $W_{m,d}$ and $W_{r,d}$. Therefore, based on Eq. (3), the non-dimensional work done by external forces W_{ext} and relevant dissipated energies are evaluated as,

$$\begin{aligned} W_{ext} &= \int_{\tau_1}^{\tau_2} f_{ext}(\alpha, \Omega, \tau)\hat{x}' d\tau \\ W_{m,d} &= \int_{\tau_1}^{\tau_2} \eta\hat{x}'\hat{x}' d\tau \\ W_{r,d} &= \lambda\eta_r \int_{\tau_1}^{\tau_2} (\hat{x}'_r - \hat{x}'_m)\hat{x}'_r d\tau - \int_{\tau_1}^{\tau_2} (\hat{x}'_r - \hat{x}'_m)\hat{x}'_m d\tau \end{aligned} \tag{11}$$

The steady-state energy values in Eq. (11) are averaged in a time window of $\tau = 250 - 500$ to include enough exchanges between kinetic, potential and driven boundary energies. Relevant ratios have been computed as,

$$\begin{aligned} EDR_B &= (W_{m,d}/W_{ext}) \times 100\,(\%) \\ EDR^R_{BwR} &= \left[(W_{r,d})/W_{ext}\right] \times 100\,(\%) \\ EDR^T_{BwR} &= \left[(W_{m,d} + W_{r,d})/W_{ext}\right] \times 100\,(\%) \end{aligned} \tag{12}$$

where the subscript BwR refers to the bistable oscillator coupled with a resonator, whilst the superscripts R and T reflect the energy dissipated in the resonator alone and in the coupled oscillator, respectively.

The ratios in (12) are plotted in Fig. 13 for $\eta_r = 0.075$, $\varphi = 2$, and $\lambda = 0.8$. Both colour maps and contour maps clearly indicate low dissipation regions at low amplitudes. When resonators are introduced, energy dissipation begins at a lower frequency compared to the standalone bistable oscillator. However, as the input amplitude increases, the energy dissipation ratio EDR of the bistable oscillator begins to rise at lower frequencies, indicating the onset of interwell motions

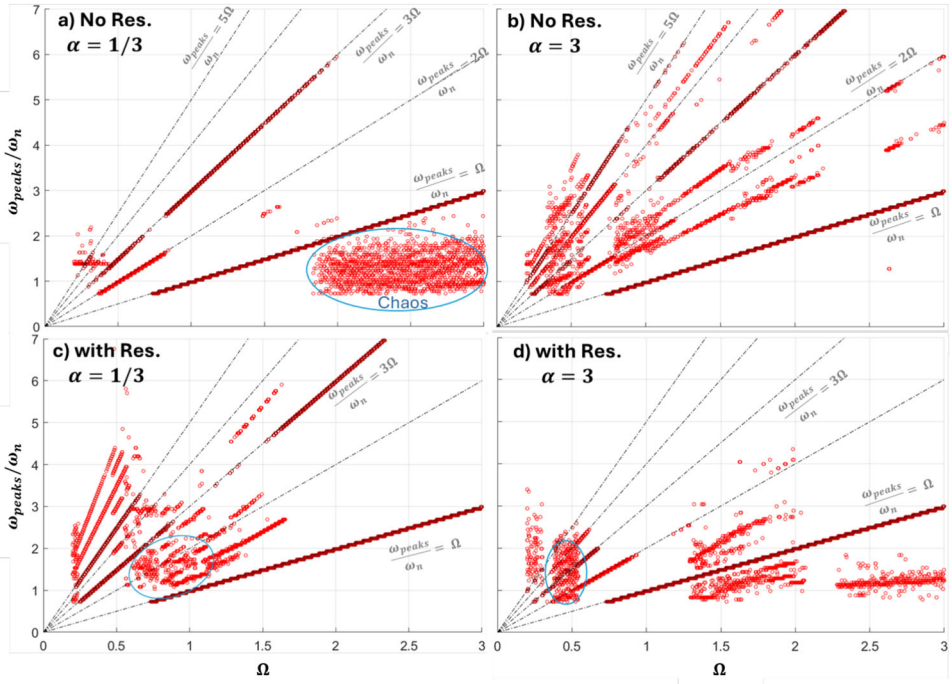

Fig. 6 Frequency peaks' (Harmonic) diffusion vs. $\Omega = \omega_0/\omega_n$ for: **a**, **b** Bistable oscillator; **c**, **d** Bistable oscillator coupled with a resonator($\varepsilon = 1, \eta = 0.1, \eta_r = 0.075, \varphi = 2, \lambda = 0.8$)

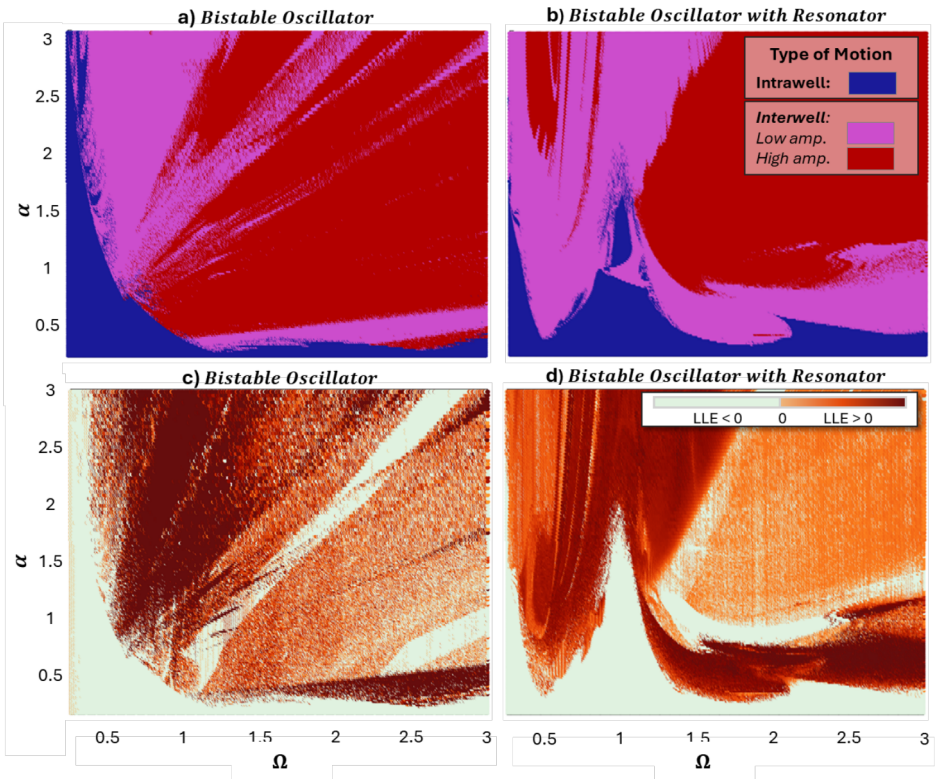

Fig. 7 Type of motion and large Lyapunov exponent (LLE) values for various input amplitudes $\alpha = A_0/\delta_s$ vs. frequency, $\Omega = \omega_0/\omega_n$ for: **a**, **c** Bistable oscillator; **b**, **d** Bistable oscillator coupled with a resonator ($\varepsilon = 1, \eta = 0.1, \eta_r = 0.075, \varphi = 2, \lambda = 0.8$)

that progressively govern the system response (see Fig. 7). Importantly and beyond its tuned frequency, the resonator is still capable of dissipating a significant amount of input energy W_{ext}; this favourable effect is associated with the harmonic diffusion and chaotic response characteristics of the bistable oscillator. When the high-frequency, low-amplitude range is examined, the energy dissipation provided by the resonator decreases significantly. However, at higher amplitudes within the same frequency range, a moderate level of dissipation is still observed. This highlights the importance of proper resonator tuning, which should account not only for the target frequency but also for the input amplitude.

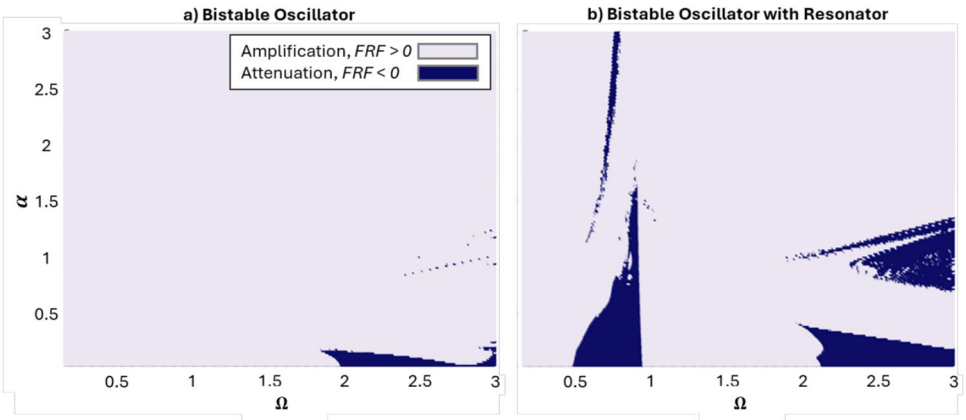

Fig. 8 Frequency response functions (FRF) plots for $\alpha = A_0/\delta_s$ vs. frequency, $\Omega = \omega_0/\omega_n$ for: **a** Bistable oscillator; **b** Bistable oscillator coupled with a resonator ($\varepsilon = 1, \eta = 0.1, \eta_r = 0.075, \varphi = 2, \lambda = 0.8$)

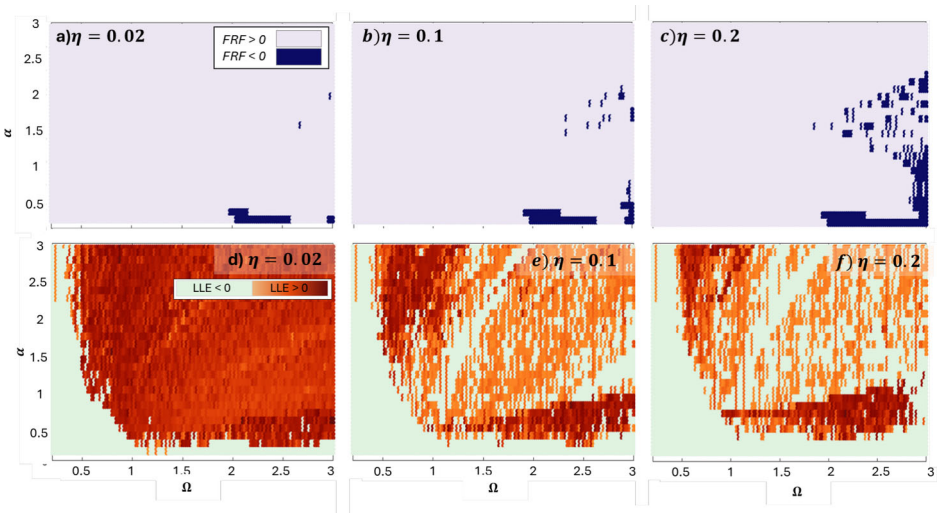

Fig. 9 FRF and LLE values of a bistable oscillator without resonator subjected to various input $\alpha = A_0/\delta_s$ and frequencies $\Omega = \omega_0/\omega_n$ and predefined $\eta = c(m\omega_n)^{-1}$ for $\varepsilon = k_3\delta_s^2(m\omega_n^2)^{-1} = 1$; **a**–**c** limited increase of attenuation zones; **d**–**f** marked increase of stable regions

4 Experimental feasibility and characterisation

In this section, both the experimental setup and the prototype of the bistable oscillator coupled with the resonator are described. For comparison and as a baseline for the experimental setup linear oscillators were also tested. Then, the main characteristics of the prototype are measured and identified.

4.1 Testing equipment and bistable oscillator mock-up

The sketch of the experimental setup is presented in Fig. 14 together with a photo of the bistable oscillator connected to a driven boundary, i.e. the shake table. The oscillators have been designed to operate in the low frequency range, i.e. up to 10 Hz with a size of approximately 10 cm in all dimensions. The characteristics of the separate parts of the oscillators are provided in Fig. 15, together with the photo of the assembled 3D printed prototype.

The excitation to the oscillators was imparted through a driven boundary, i.e. in displacement control, which has been provided by a compact shaking table as sketched in Fig. 14a, b. The shake table provided input profiles with a maximum velocity of 0.5 m/s. The oscillators were made of 3D printed parts that were assembled to realise the main cell and the resonator, where the cell represents the main mass. The springs and dampers of the main cell were reproduced with beams working in simple shear. The beam ends were rotationally constrained, and the experiment was designed to run on a single axis (X) only; therefore, circular aluminium rails were considered in parallel to the shake table for the attachment of the main cell and resonators using linear bearings, as depicted in Fig. 14. Damping forces were naturally obtained from the inherent damping and friction in the 3D manufactured parts.

The model of the main cell, that is, the frame, is presented in Fig. 15a. The void in the cell is meant for the resonator. The truss supports at the top of the main cells were added to resist rotational deformations in the X direction. In case of bistable oscillator, the frame was connected to the shake table using bistable beams (Fig. 15a-iii). The compressive load required for beam buckling was achieved

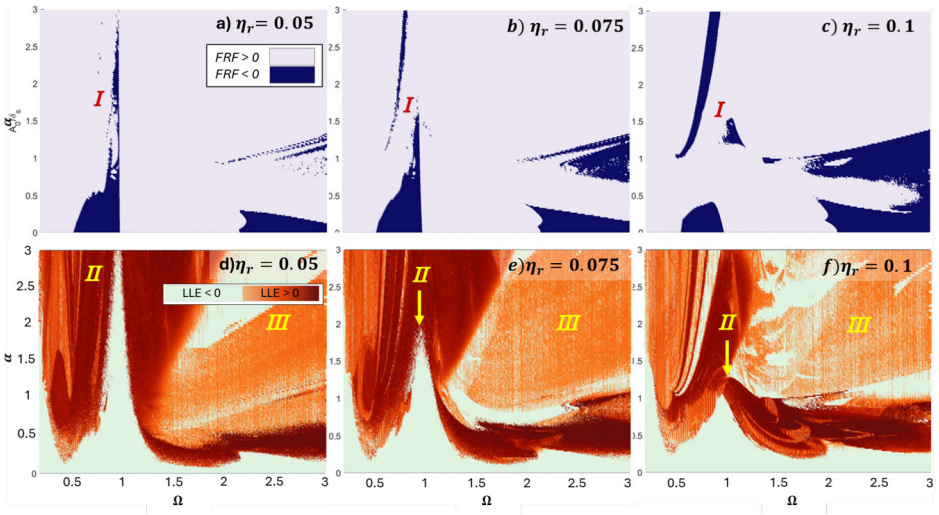

Fig. 10 FRF and LLE values of a bistable oscillator coupled with a resonator subjected to various input $\alpha = A_0/\delta_s$ and frequencies $\Omega = \omega_0/\omega_n$ and predefined $\eta_r = c_r(m_r\omega_n)^{-1}$ for $\varepsilon = 1$, $\eta = 0.1$, $\varphi = 2$, $\lambda = 0.8$; **a–c** marked increase of attenuation; and **d–f** limited reduction of stable regimes

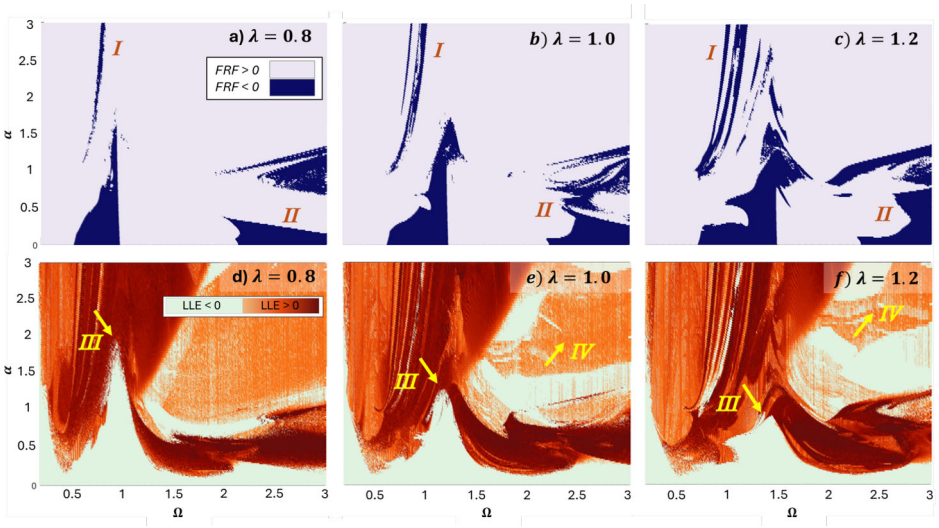

Fig. 11 FRF and LLE values of a bistable oscillator coupled with a resonator subjected to various input $\alpha = A_0/\delta_s$ and frequencies $\Omega = \omega_0/\omega_n$ for predefined λ, where $\omega_r = \sqrt{k_r/m_r} = \lambda\omega_n$ for $\varepsilon = 1$, $\eta = 0.1$, $\eta_r = 0.075$, $\varphi = 2$: **a–c** limited increase of the attenuation zones; **d–f** limited increase of stable zones

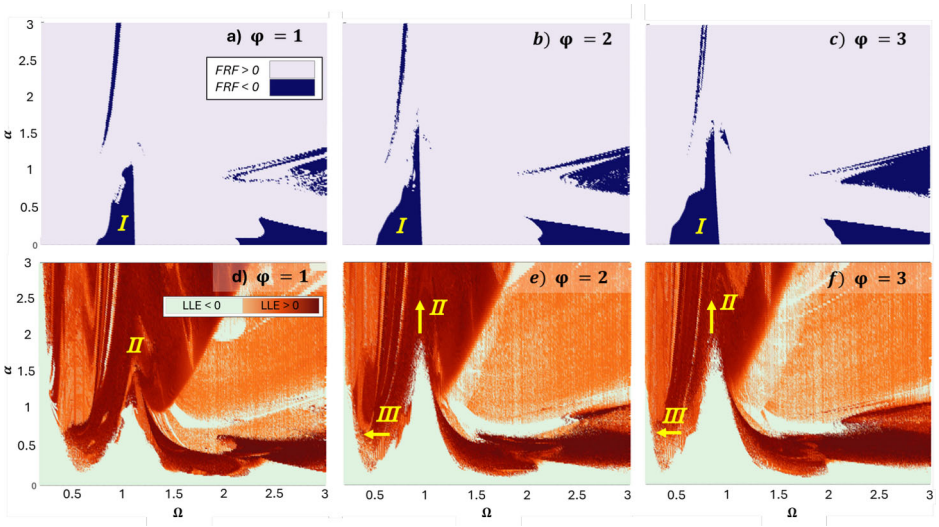

Fig. 12 FRF and LLE values of a bistable oscillator coupled with a resonator subjected to various input $\alpha = A_0/\delta_s$ and frequencies $\Omega = \omega_0/\omega_n$ and predefined values of φ, where $m_r = m_m\varphi$ for $\varepsilon = 1$, $\eta = 0.1$, $\eta_r = 0.075$, $\lambda = 0.8$: **a–c** limited increase of the attenuation zones; **d–f** limited increased of the steady-state responses

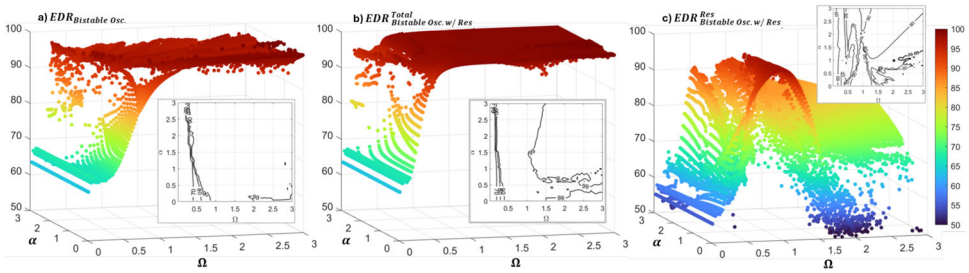

Fig. 13 Energy dissipation ratio values and contour maps relevant to various input amplitudes $\alpha = A_0/\delta_s$ and frequencies $\Omega = \omega_0/\omega_n$, for $\varepsilon = 1, \eta = 0.1, \eta_r = 0.075, \varphi = 2, \lambda = 0.8$: **a** Bistable oscillator, EDR_B; **b** total of bistable oscillator with resonator, EDR^T_{BwR}; and **c** resonator alone, EDR^R_{BwR}

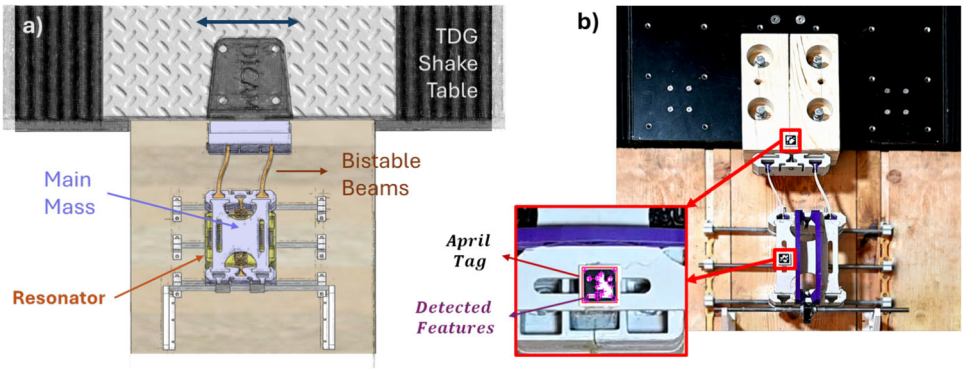

Fig. 14 **a** Schematic of the experimental setup; **b** Photo of the setup with the bistable oscillator endowed with 3D printed April tags for feature detection

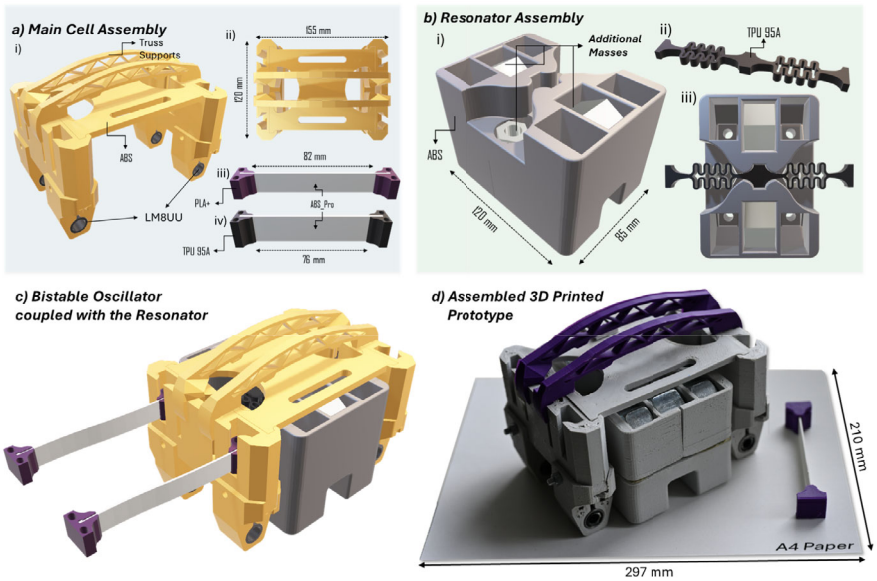

Fig. 15 **a** Characteristics of the main cell and beams (i:perspective view, ii: top view, iii: bistable beam and iv: linear beam); **b** Details of the resonator (i:perspective view, ii: resonator beam, iii: top view; **c** Assembled bistable oscillator coupled with the resonator; **d** Assembled 3D printed prototype with the underneath A4 paper

by using beams longer than the default distance. The design of the bistable beams, together with force-displacement relationships obtained through a finite element analysis (FEA), are provided in Fig. 16a. FEA were performed using COMSOL Multiphysics[43]. The beam model accounted for the interaction between the components, which were assumed to be perfectly bonded. The bottom end of the beam was fully fixed, and displacements were measured at the top end which was rotationally constrained. A two-step analysis procedure was employed. In the first step, a stationary study with displacement control in the longitudinal direction was performed until the displacement reached –6 mm, corresponding to the gap between the main cell and the shaker table support. Once the target displacement was achieved, a second step involving lateral displacement-controlled analysis was conducted, from which the force–displacement response

shown in Fig. 16a was obtained. For the numerical solution, the PARDISO direct linear solver was used in combination with the automatic Newton–Raphson nonlinear solver built into COMSOL. The maximum number of nonlinear iterations was increased to ensure convergence under strong geometric nonlinearities. A physics-controlled "Finer" mesh was applied to balance accuracy and computational cost. For the so-called linear oscillators, non-buckled beams operating in shear, as in bistable case, were used (Fig. 15a-iv). It is acknowledged that these beams may exhibit geometric nonlinearities under large displacement. However, given their high slenderness ratio and the limited deformation range within the test setup, such effects remain negligible. Therefore, the term "linear beam" is used throughout the manuscript for brevity.

Details of the resonator design are provided in Fig. 15b. Each resonator is connected to a linear cylindrical aluminium rail with a SK8UU bearing from the middle-bottom as sketched in Fig. 14. To obtain additional weight, each resonator was modified to tightly embed steel nuts. The reader can observe from 15c, that the distance between each main cell and the relevant resonator is limited; this restricts the beam length for the resonator to the main cell and results in additional second-order effects. In fact, standard rectangular beams were unable to exhibit linear behaviour due to strong non-linear hardening, as shown in Fig. 16b. Therefore, an improved resonator beam design capable of accommodating large lateral displacements of the resonator without second-order effects was conceived. FE analyses of both rectangular and enhanced designs can be appreciated in Fig. 16b, where the reader can observe the more favourable stress distribution within the $\pm$ 5 mm range. In comparison to the FEA performed for the bistable beams, the analysis of the resonator beams was carried out using a single-step, displacement-controlled stationary study. Both ends of the beam were fully fixed, and a displacement-controlled load was applied along the symmetry axis, as illustrated in Fig. 16b.

4.2 Materials, manufacturing and identification

As mentioned in Sect. 1.1, the parts were manufactured by 3D printing with the FDM technique, which provided flexibility for both the main cell, the resonator and the beams. Therefore, both the design and manufacturing were made in-house, with available Fused Filament Fabrication (FFF) 3D printers, a subclass of FDM. Moreover, the design of the components was carried out looking for supportless printing and reducing waste.

With regard to manufacturing, all components apart from springs, i.e. beams, were manufactured by acrylonitrile butadiene styrene (ABS) material; in fact, ABS is characterised by high toughness and resistance for mechanical applications, thus providing sufficient stiffness and durability. For ease of printing and durability, the inter-cell beams were printed in 3 parts: the centre piece and two end connections as indicated in Fig. 15c. To achieve greater flexibility and fatigue resistance, the central part of these beams was printed using ABS and polycarbonate (PC) composite filament. Moreover, to prevent stress localisation near the connections, end connections of linear beams were printed using thermoplastic polyurethane (TPU) material. In the case of bistable beams, instead ABS was preferred, since stress localisation was not a concern, as observed from the aforementioned FE analyses. To achieve low stiffness, TPU was also used for the beams employed in the resonators. The mechanical properties for all materials involved were provided by filament manufacturers and are collected in Table 1. The Cubic infill at 20% was considered for ABS used in all components, whilst beams were printed with 100% infill.

The mechanical properties of the main cells and beams were statically identified with a 10 cm LVDT and a miniature load cell with a capacity of 500 N. Dynamical identification was used for the beams of the resonators, by means of a high-speed and high-resolution SLR camera together with digital image correlation (DIC). In particular, 1920 by 1080 pixels, 120 frames per second videos were recorded and analysed. Since experiments required multiple object recognition, that is, input and output, and accuracy tracking, AprilTags [44], which were also 3D printed using black and white PLA filaments for high contrast and resistance to bending, were located on top of the shake table and cells. For high performance and minimum false-positives, tags from the -tag36h11- family were used. During post-processing, each frame of the videos was corrected for pre-computed intrinsic and lens distortion parameters of the camera. In the undeformed series of cells, each tag was recognised and the corner features were extracted using the minimum eigenvalue algorithm [45]. Although the last step is not mandatory, it performed better with high robustness against motion blur and noise. The extracted features were tracked by means of the Kanade-Lucas-Tomasi feature-tracking algorithm [46]. Since each tag dimension was known, pixel-based tracking results were converted to actual displacements. The test setup together with the attached AprilTags and an example of detected features are given in Fig. 14b.

5 Identification of unit cell mechanical properties

The identification of mechanical properties of the unit cell was based on considering the following system of EoMs for one bistable oscillator coupled with a resonator,

$$\mathbf{M}\ddot{x} + \mathbf{F}_d(x)\dot{x} + \mathbf{F}_f(\dot{x}) + \mathbf{F}_k(x) = \mathbf{F}_{ext}(\omega, t) \tag{13}$$

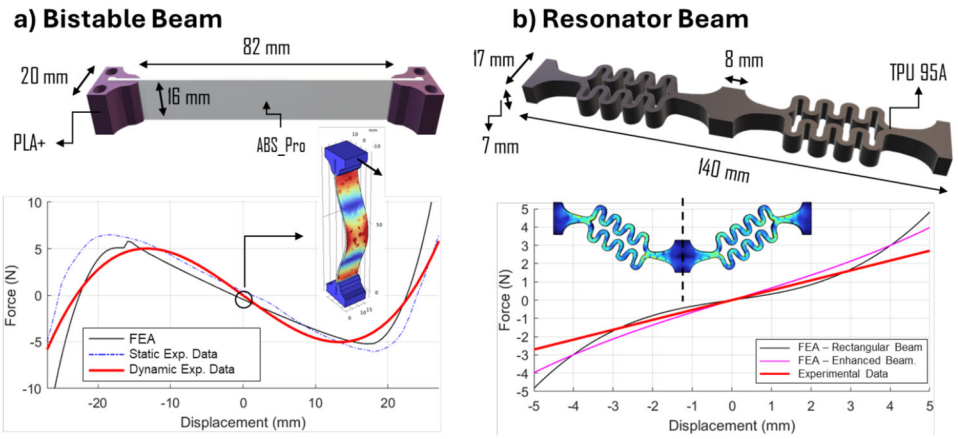

Fig. 16 Designs of the bistable beam (**a**) and the resonator beam (**b**), accompanied by FEA results and experimental validation demonstrating their mechanical response under lateral force. (For the bistable beam, displacements were measured at the top end, with the bottom end fully fixed. For the resonator beam, displacements were measured along the symmetry axis–dashed line–while both beam ends were fully fixed)

Table 1 Properties of materials used for 3D FFF printing

Material	Components	Density kg/m^3	Elastic Modulus MPa	Tensile Strength MPa	Print Temp $^\circ C$
ABS + PC	Main beams	1.02	2100	40	260
TPU	Resonator beams*	1.16	150	50	230
ABS	Others	1.10	2030	43.6	250

where $\mathbf{F}_d(x)$, $\mathbf{F}_f(\dot{x})$, $\mathbf{F}_k(x)$, and $\mathbf{F}_{ext}(\omega, t)$ define external damping, friction, nonlinear elastic, and external forcing matrices. The matrices involved in (13) read,

$$\mathbf{M} = \begin{bmatrix} m_m & 0 \\ 0 & m_r \end{bmatrix} \tag{14}$$

$$\mathbf{F}_d(x) = \begin{bmatrix} c_{m,0} & -c_{r,0} \\ -c_{r,0} & c_{r,0} \end{bmatrix} + \begin{bmatrix} c_{m,2} & -c_{r,2} \\ -c_{r,2} & c_{r,2} \end{bmatrix} |x|^2 \tag{15}$$

$$\mathbf{F}_f = \begin{bmatrix} F_{f,m}(\dot{x}) & 0 \\ 0 & F_{f,r}(\dot{x}) \end{bmatrix} \tag{16}$$

$$\mathbf{F}_k = \begin{bmatrix} k_1 & -k_r \\ -k_r & k_r \end{bmatrix} x + \begin{bmatrix} k_3 & 0 \\ 0 & 0 \end{bmatrix} x^3 \tag{17}$$

where the subscripts m and r refer to the main cell and the resonator, respectively. The term, F_k involves a cubic polynomial that simulates the bistable beam with $k_3 > 0$, and $k_3 = 0$ for a linear beam. For an accurate representation of damping, both dry kinetic and static friction were also included. More specifically, the dry friction term, F_f was modelled following the formulation proposed by Specker et al. [47] that reads,

$$F_f(\dot{x}) = \left(F_{f,s} - F_{f,k} \tanh(xsp/xvt)\right) g_f + F_{f,k} \tanh(x/xvt)\Big) g_f + F_k \tanh(\dot{x}/\dot{x}_{vt}) \tag{18}$$

$$g_f = \frac{\dot{x}}{\dot{x}_{sp}} exp\left(0.5 - \left(\frac{\dot{x}}{\sqrt{2}\dot{x}_{sp}}\right)^2\right) \tag{19}$$

where $F_{f,s}$ and $F_{f,k}$ define the static and kinetic friction-induced force, and constants $\dot{x}_{sp}$ and $\dot{x}_{vt}$ refer to Stribeck peak velocity and transition velocity, respectively, depicted in Fig. 17; the difference between Coulomb friction and Eqs. 18-19 can be understood from the same Fig. 17. Low $\dot{x}_{sp}$ and $\dot{x}_{vt}$ values result in sharp behaviour and numerical difficulties for sampling at ultra-low frequencies.

The masses of the main cell and the resonator amounted to $m_m = 0.282\ kg$ and $m_r = 0.620\ kg$, respectively. The force-displacement relationship for inter-cell beams was also measured quasi-statically; therefore, the stiffness value of the linear beams read $k_1 = 350 \pm 20\ N/m$ as indicated in Fig. 16b. For the bistable beam, the measured force-displacement relationship is provided in Fig. 16c and the relevant values read $k_1 = -1137 N/m$ and $k_3 = 1.86e6\ N/m^3$.

With regard to dynamic measurements, it must be noted that, due to low stiffness and mass values of the components, the measuring devices could have a noticeable impact on the results. Consequently, contactless measurements with dynamic identification approaches were deemed to be more reliable.

To identify the parameters $k_1, k_3, c_0, c_2, F_{f,s}, and F_{f,k}$, and reduce the risk of wrong identification values due to response non-uniqueness [40], multiple frequency sweep-driven boundary excitations were applied to the oscillators. The main oscillator was tested both stand-alone and coupled with a resonator, and displacement/velocity data of both the shake table and the oscillator were recorded. The frequency

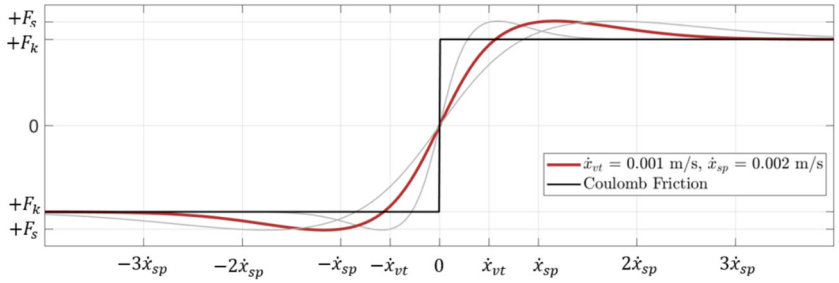

Fig. 17 Friction forces exerted for various peak velocity $\dot{x}_{sp}$ and transition velocity $\dot{x}_{vt}$ values

content of each velocity response was calculated by means of the fast Fourier transform (FFT), $V_{n,1}(f)^{ex}$.

The numerical model of the oscillator was subjected to the input displacement histories provided by the shake table tag. The numerical responses of the oscillators were obtained using an explicit Runge–Kutta integrator, whilst the constants $\dot{x}_{sp}, \dot{x}_{vt}$ in Eqs. (18) and (19) were taken as 0.002 and 0.001 m/s, respectively. Successively, the parameters of the aforementioned damping model were determined by the least square error between the numerical $V_{n,1}(f)^{nu}$ and the experimental $V_{n,1}(f)^{ex}$ FFT values. The minimisation then corresponds to a multivariate optimisation problem where the objective function has been defined as:

$$\min \left[\frac{1}{n_s n_k} \sum_{k=1}^{n} \sqrt{\left(\sum_{f=0}^{f_k} \left| v_{n,1}(f)^{nu} - v_{n,1}(f)^{ex} \right|^2 \right)} \right] \quad (20)$$

where n_s and n_k are the number of sweeps considered and number of discrete frequencies at the k^{th} sweep. For brevity, mean values were considered, and the optimisation problem was solved by a genetic algorithm, with an initial population size of 600 and a crossover fraction of 0.6, for a more aggressive exploration of the search space. Identified results are collected in Table 2.

The best approximation of parameters was achieved in the stiffness terms, as these parameters were readily approximated from quasi-static tests, see Fig. 16c, d; or they were identified from the FRF responses in the case of resonators, as indicated in both Figs. 18 and 19. Moreover, in the linear case, the FRF peak corresponds to the resonance frequency of the system; whilst in the case of the bistable cell, the linear component of $f_k(x)$ was obtained from the low-amplitude response, by peak matching, whilst the cubic term, k_3, was computed from the distances between stable states.

Notably, for the linear case, the numerical model described by Eq. 13 endowed with the optimised parameters of Table 2, was overall capable of accurately reproducing experimental results; this is evident in Fig. 18. The same trend was observed for the bistable oscillator responses depicted in Fig. 19. Nonetheless, in the high-frequency regions, it was observed that a minor change in the value of k_3 could drive the system to chaos, resulting in a discrepancy between numerical and experimental results.

To further verify the identification parameters of the bistable oscillator, frequency sweeps conducted with $A_0 = 6\ mm$ and $A_0 = 9\ mm$ and relevant comparisons are provided in Fig. 20. It is important to acknowledge that these sweeps were not part of the identification process.

Overall, the identified parameters entailed a good accuracy in predicting the FRF provided by the experimental outcomes, with one notable exception in Fig. 20a: the experiment response resulted in an aperiodic response, whilst the numerical observation did not result in aperiodicity. This discrepancy was attributed to two sensitivities: (i) the magnitude of the Stribeck peak velocity $\dot{x}_{sp}$ [47]; and (ii) the accuracy of the numerical solver. In an attempt to address the former issue, adjustments were made by lowering $\dot{x}_{sp}$. However, the integration process became inefficient or excessively time-consuming, hence a trade-off was made.

6 Experimental results and comparisons

The experimental results provided by the system analysed in Sect. 5 with one cell and complemented with the results of two cells are shown and discussed here. They are compared with the numerical analysis results based on the identified parameters collected in Table 2.

6.1 Comparisons between experimental data and numerical predictions

The FRFs experimental data computed for various sinusoidal inputs are presented in Fig. 21, and are compared with the numerical results of linear and bistable oscillators.

Specifically, in the case of the main cell endowed with linear beams and without a resonator, see Fig. 21a, the numerical model closely mirrors experimental data with marked differences in the high-frequency range. The discrepancy at high frequencies can be attributed to increased velocities and displacements, which induce higher-order effects due to large displacements and hardening.

In the case of the bistable oscillator with a resonator, Fig. 21b, to capture the response in the high-frequency

Table 2 Identified parameters for bistable and linear oscillator prototypes

	m kg	f_{init} Hz	k_1 N/m	k_3 N/m^3	c_0 Ns/m	c_2 Ns/m^3	$F_{f,s}$ N	$F_{f,k}$ N
Linear Osc	0.282	6.6	484.9	–	3.2	8.9 e3	1.2	0.65
Bistable Osc	0.282	10.1	1135.7	2.15e6	1.5	8.6e3	1.2	0.44
Resonator	0.620	5.1	636.6	–	4.6	38.7 e3	1.4	0.59

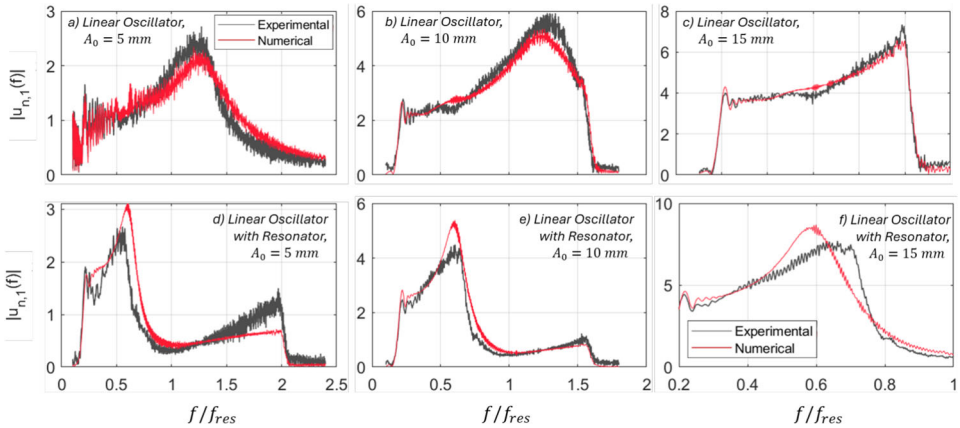

Fig. 18 Comparison between experimental and numerical frequency sweeps used during the identification process. **a**–**c** linear oscillator responses; and **d**–**f** linear oscillator responses coupled with a resonator. The x-axes are normalised with respect to the resonator frequency, i.e. 5.1 Hz

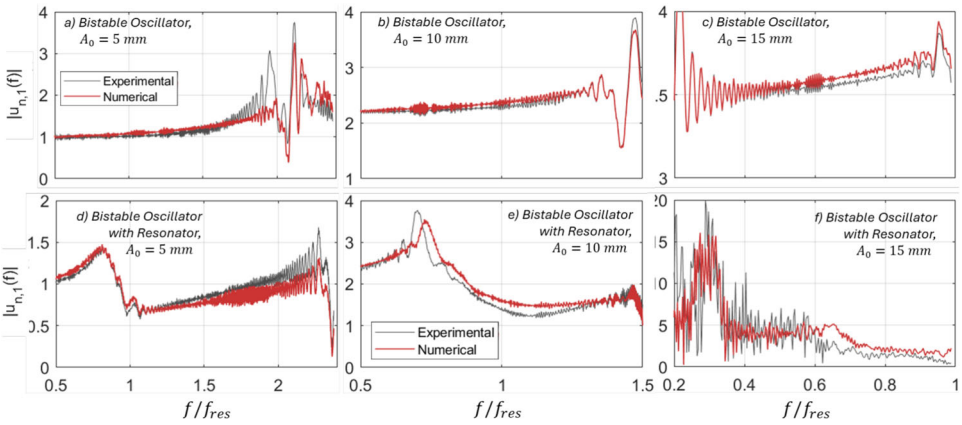

Fig. 19 Comparison between experimental and numerical frequency sweeps used during the identification process. **a**–**c** bistable oscillator responses; and **d**–**f** bistable oscillator responses coupled with a resonator. The x-axes are normalised with respect to resonator frequency, i.e. 5.1 Hz

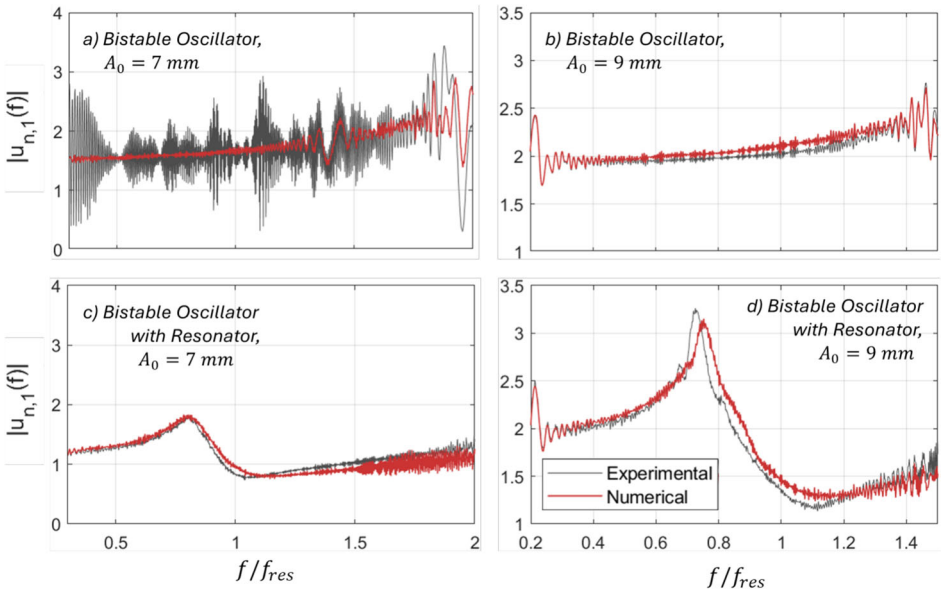

Fig. 20 Comparison between experimental and numerical frequency sweeps **not** employed during the identification process. **a**–**c** bistable oscillator responses; and **d**–**f** bistable oscillator responses coupled with a resonator. The x-axes were normalised with respect to resonator frequency, i.e. 5.1 Hz

branch, the input frequency was set slightly below the resonator frequency f_{res}, i.e. at 4.9 Hz. Results are presented for increasing input amplitudes and, aside from the amplitude near the transition to the high-energy branch, the accuracy remains satisfactory. Notably, at $A_0 = 11\,mm$, numerical results converge to the lower branch, whereas in the experiment, high-energy interwell motions are observed. This behaviour underlines the challenges discussed in Sects. 3 and 5 regarding the prediction of a system characterised by chaotic motion.

Further examination of results for the stand-alone bistable oscillator, see Fig. 21c–e, reveals the approximation reached with various input amplitudes. Moreover, due to shaking table limitations, experimental results fail to accurately capture high-energy branches. Nonetheless, good results are achieved for other amplitude ranges.

6.2 Frequency sweep results

Figure 22 illustrates the response of a bistable oscillator, both uncoupled and coupled with a resonator, to a frequency sweep input ranging from 1 to 8 Hz with $A_0 = 10\,mm$ and rate of 0.06 Hz/s. It should be noted that the system behaviour is inherently sensitive to both the sweep rate and its direction. The selected rate was chosen to be as low as practically achievable, to minimise the dynamic effects caused by sweep rate, within the limitations of the experimental setup. Furthermore, a slightly reduced actual amplitude can be observed in the measurements, which is attributed to minor variations in the shake table response, the measurement system and mechanical tolerances in the experimental setup. Nonetheless, for the numerical models, the measured input signals from the shake table were used; therefore, this reduction does not affect the validity of the results. For simplicity and consistency, the nominal input values commanded to the shake table are reported throughout the paper. The response of the bistable oscillator without resonator follows the input as indicated in Fig. 22b; nonetheless, the impact of the resonator on the oscillator's response is evident from Fig. 22c, as the response amplitude decreases when the input frequency approaches the resonator frequency, i.e. ($f_{res} = 5.1\ Hz$).

To provide an additional insight, the FFT was applied to the responses, and the frequency content of both input and output signals is depicted in Fig. 23, for linear and bistable oscillators coupled with a resonator.

For clarity, the results are normalised to the frequency of the resonator ($f_{res} = 5.1\ Hz$). FFT values for both input and output are presented alongside their FRF ratios in decibels (dB). The attenuation effect entailed by the resonators is distinctly observed in both cases around f_{res}. Whilst the linear oscillator exhibits higher attenuation at f_{res}, reaching about -12 dB; it also exhibits a peak response of 9 dB. Conversely, the FRF peak value of the bistable oscillator remains below 5 dB, demonstrating the benefits of bistability.

Based on the considerations of Sect. 2, it was shown that the response of the bistable oscillator depends on the input amplitude. Accordingly, different amplitude values, i.e. $A_0 = 5\,mm$ and $A_0 = 15\,mm$ were imposed to the oscillator. Relevant results are presented in Fig. 24. For high input amplitudes, the FFT spectrum becomes broadly distributed over multiple frequencies without a dominant peak. This broadband energy distribution indicates complex, potentially chaotic dynamics. In particular, compared to low-amplitude inputs, the distinction between background noise and aperiodic system response is clearly observed. With regard to attenuation, it starts at $0.85\,f_{res}$ in the low amplitude case, see Fig. 24a; conversely, the attenuation begins at $0.6\,f_{res}$ for the high amplitude case and is maintained. Thus, the advantage of interwell motion is clear in terms of attenuation, though chaos can be a drawback. In addition, in Fig. 24, also time-frequency analyses were conducted and spectrogram results are given. In case of $A_0 = 5\,mm$, the spectrogram shows a clear diagonal line from low to high frequency over time, corresponding to the frequency sweep of the input. The spectral content is mostly concentrated along this line, indicating that the system response is dominated by periodic motion following the input frequency. Minor energy spread around the diagonal was observed, due to inherent damping, but overall, the response is narrowband and consistent with the expected response for low amplitude. Around $t = 20 - 40\,s$, corresponding to $0.7\,f_{res} - 0.9\,f_{res}$ region in FFT plot, weak harmonics were observed; since the nonlinearity in the system start to be more dominant as response amplitude increases. In case of $A_0 = 15\,mm$, the diagonal is still visible, but now a broader band of energy appears above and below the diagonal, particularly at higher frequencies, i.e. ($t > 30\,s$). This indicates the interwell motion and chaotic response, where energy is distributed across multiple frequencies rather than concentrated at the input frequency. The increased spectral richness matches the FFT observation at low frequencies. Spectrograms clearly indicate the transition from simple periodic motion at low frequencies to complex, multi-frequency dynamics at higher frequencies.

6.3 Two oscillators in series

To enhance our knowledge of bistable systems in series and to corroborate previous research conducted on bistable metafoundations with two layers [32], additional experiments were undertaken. They involved two oscillators in series both uncoupled and coupled with resonators. Test setup and relevant results are presented in Fig. 25, noting that results on the left correspond to the 1st oscillator whilst those on the right correspond to the 2nd oscillator w.r.t. the shaking table.

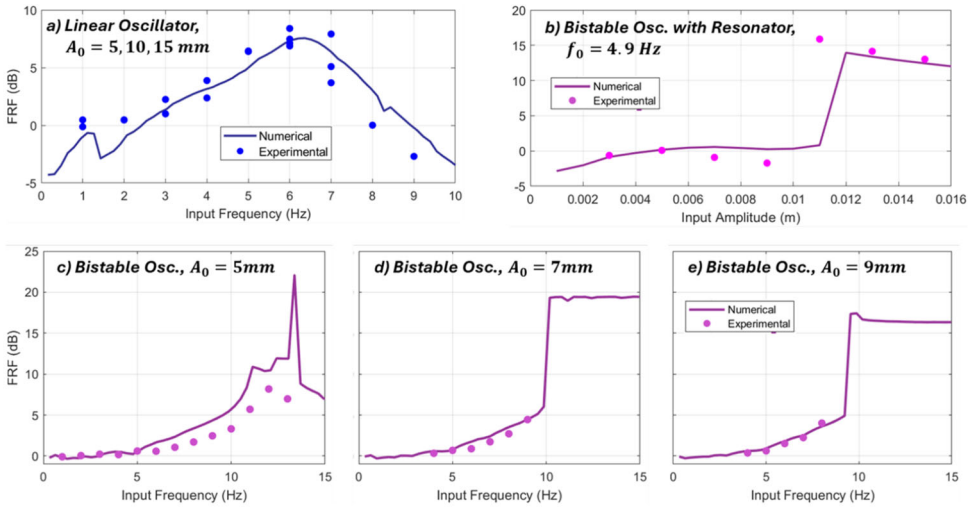

Fig. 21 Frequency response results for sinusoidal — $A_0 sin(f_0 t)$ — driven base input: **a** linear oscillator subjected to $A_0 = \{5, 10, 15\}$ mm and $f_0 = 1 - 9\ Hz$ inputs; **b** bistable oscillator with resonator subjected to $A_0 = \{1 - 15\}$ mm and $f_0 = 4.9\ Hz$; and **c**–**e** bistable oscillator subjected to $A_0 = \{5, 7, 9\}$ mm inputs with various frequencies. The input frequency and amplitude was limited to $A_0 f_0 < 0.5$

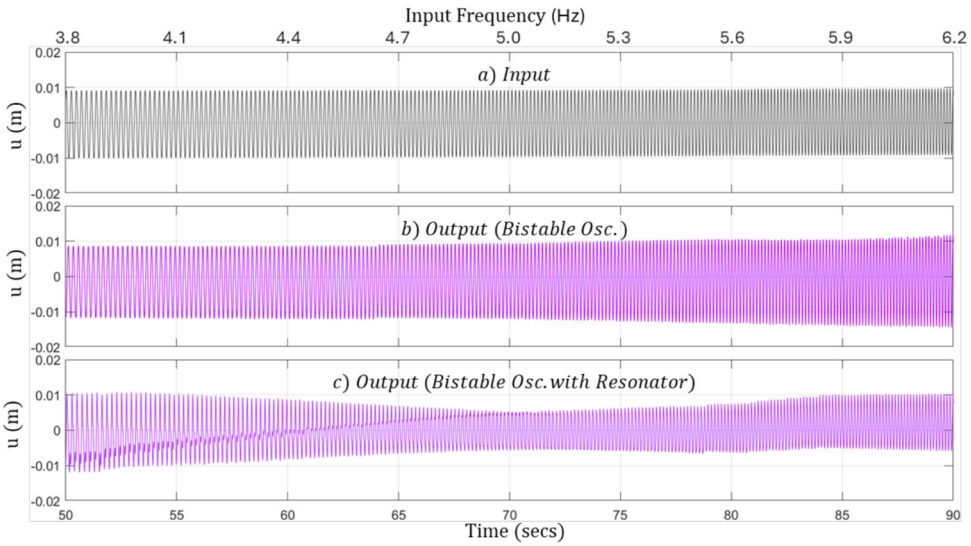

Fig. 22 Time history responses to frequency sweeps: **a** input at constant amplitude; **b** response of the bistable oscillator; **c** response of the bistable oscillator with resonator

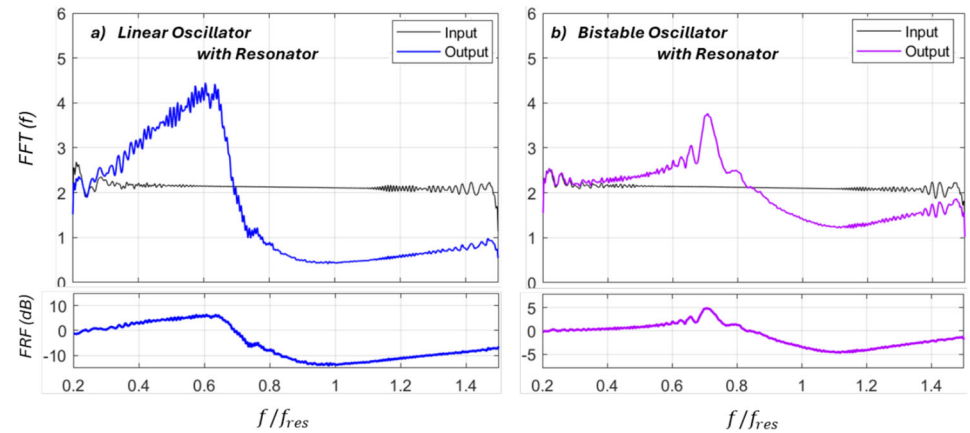

Fig. 23 Comparison between experimental results in the frequency domain obtained from: **a** the linear oscillator with resonator; **b** the bistable oscillator with resonator subjected to frequency sweep ($A_0 = 10\,mm$, $f_0 = 1 - 8Hz$). FRF values represent the ratio between output and input values, and negative values mean attenuation

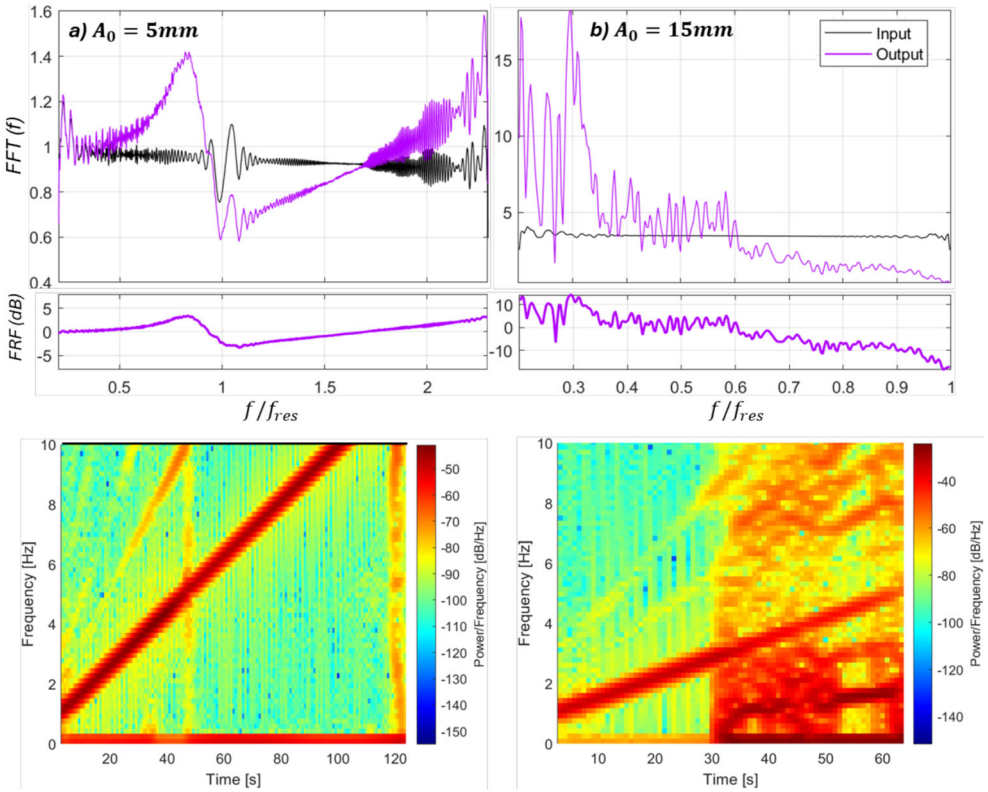

Fig. 24 Comparison between experimental results in the frequency domain for the bistable oscillator with resonator subjected to frequency sweeps with: **a** $A_0 = 5\,mm$, $f_0 = 1 - 12Hz$; **b** $A_0 = 15\,mm$, $f_0 = 1 - 5Hz$. FRF values represent the ratio between output and input values, and negative values mean attenuation. A spectrogram is provided to illustrate the time-frequency response and the regions of aperiodic response

Overall, the results are in line with expectations and extend the understanding of bistable–resonator interactions to multi-oscillator configurations. Notably, the presence of a second oscillator led to attenuation starting at a lower frequency, thus resulting in improved performance compared to the single oscillator case. A careful reader can notice in the last part of the simulation for the case of the stand-alone bistable oscillators, see Fig. 25c, the clear transition from intrawell to interwell motion with an evident displacement amplification. This transition does not occur with the presence of resonators, as clearly understood from Fig. 25d.

Such bistable oscillators in series experiments reflect configurations studied in recent metafoundation research [32] where bistable columns in multi-layer foundations show enhanced mitigation of vibrations under seismic loading. This work illustrate that increasing the number of bistable elements or combining bistable units in series can lower the effective frequency range for attenuation, improve energy dissipation, and introduce richer nonlinear dynamics, that can be tuned with the presence of resonators. This establishes a valuable link between the current single-unit investigation and prospective applications in metastructure and metamaterial design.

7 Conclusions and future perspectives

In this work, the fundamental problem of a damped bistable system coupled with a linear resonator and excited by a driven boundary has been explored. It has been clearly found that the system is characterised by complex responses that depend on the system and excitation parameters. To realise a bistable behaviour, slender beams buckled under axial compression were considered. An analytical solution for the proposed oscillator was derived, under the assumption of periodic responses, with solutions characterised by multiple harmonics. Clearly, the resonator has prevented transitions from intrawell to interwell motions near its tuned frequency range. However, the complexity of the system response also including bifurcations and chaotic responses, did not allow a rigorous theoretical description of the bistable oscillator. Thus all conclusions are based only on observations from simulations and experiments.

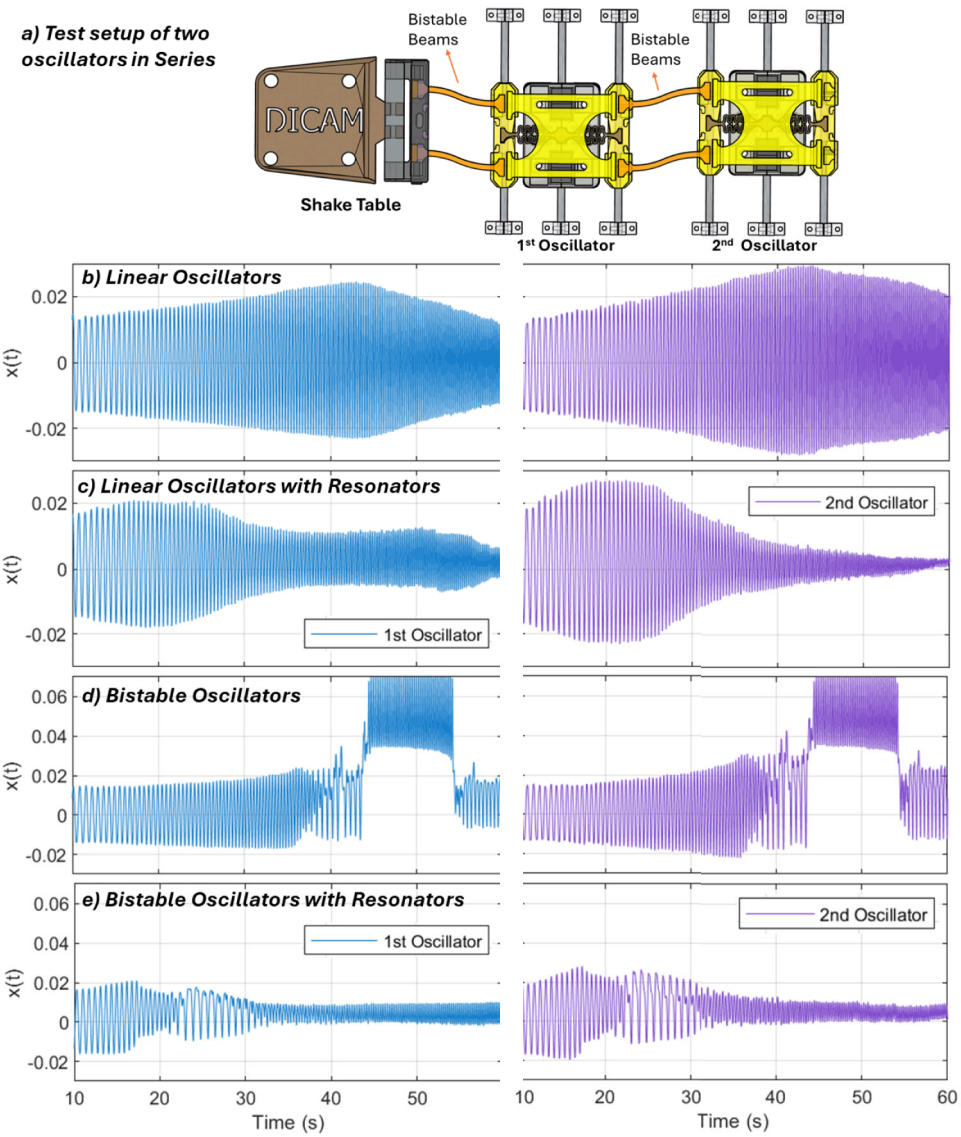

Fig. 25 **a** Test setup for two oscillators in series and; response time histories to a frequency sweep with $A_0 = 15\ mm$, $f_0 = 1 - 5\ Hz$. **b** Linear oscillators only; **c** linear oscillators coupled with resonators; **d** bistable oscillators only; **e** bistable oscillators coupled with resonators. Results on the left correspond to the 1st oscillator; those on the right correspond to the 2nd oscillator results w.r.t. the shaking table

Computational models validated on experimental results clearly demonstrated the anti-resonance effects of the resonators. Moreover, the presence of resonators provided greater confidence in predicting regions of chaotic response in terms of the input frequency-amplitude domain. With regard to energy transmission and dissipation, the resonator coupled with the bistable oscillator can dissipate a significant portion of the input energy at high frequencies w.r.t. the linear oscillator, entailing benefits well above its tuned frequency. In contrast, in the linear case, the resonator does not dissipate a significant amount of energy above its working range.

Along the lines of co-creation and community-based developments, 3D-printers were used to manufacture both the test equipment and mock-ups with inexpensive materials. To achieve bistability, the beams were subjected to axial compression at the onset of their critical buckling load. The relevant results indicated that numerical simulations cannot accurately represent the experimental findings when an aperiodic response is present. Moreover, the experimental study also highlighted that an accurate numerical model of an actual bistable oscillator requires taking into account relatively complex friction and damping forces. In addition, the response of the bistable oscillator is highly sensitive to test

conditions, parameter values, and solver tolerances, in agreement with chaos phenomena.

The key outcome of this study is that coupling a bistable oscillator with a tuned linear resonator fundamentally modifies its dynamic response, transforming comparatively unpredictable chaotic responses into controlled vibrations. This finding provides new physical insight into how linear attachments can stabilize or tune bistable and multistable systems. The aforementioned findings suggest that further research is needed to implement and realise bistable systems both standalone and coupled with resonators for targeted frequencies. Experiments are quite demanding due to the unpredictable nature of chaotic dynamics; and the more so, both aperiodic and interwell regimes challenge the robustness of numerical models. With regard to the coupling of bistable oscillators with resonators, the outcomes are positive, especially in the area of chaos prediction. To enhance the effectiveness of bistability and expand its use within finite lattice metastructures, future investigations need to explore configurations involving multiple bistable oscillators, with or without resonators. Finally, multiple bistable oscillators with series or parallel configurations may benefit from properly designed randomness.

Author Contributions T. G.: Conception, Methodology, Software, Formal analysis, Writing– original draft, Experiment, Validation. O. S. B.: Conception, Methodology, Writing– review & editing, Supervision, Resources. A. M.: Conception, Writing– review & editing, Supervision. A. P.: Conception, Writing– review

Funding The first two authors acknowledge the Italian Ministry of Education, Universities, and Research (MUR) in the framework of the project DICAM-EXC (Departments of Excellence 2023–2027, grant L232/2016). The second author also acknowledges the National Project MUR PNRR M4C2-CN1-SPOKE 9.

Data Availability Data sets generated during the current study are available from the corresponding author on reasonable request.

Declarations

Conflict of interest The authors declare no conflict of interest.

References

1. Fang, S., Zhou, S., Yurchenko, D., Yang, T., Liao, W.-H.: Multistability phenomenon in signal processing, energy harvesting, composite structures, and metamaterials: a review. Mech. Syst. Signal Process. **166**, 108419 (2022). https://doi.org/10.1016/j.ymssp.2021.108419
2. Harne, R., Wang, K.: Harnessing Bistable Structural Dynamics: For Vibration Control. Energy Harvesting and Sensing. Wiley, New York (2017). https://doi.org/10.1002/9781119128052
3. Cao, Y., Derakhshani, M., Fang, Y., Huang, G., Cao, C.: Bistable structures for advanced functional systems. Adv. Func. Mater. **31**(45), 2106231 (2021). https://doi.org/10.1002/adfm.202106231
4. Shan, S., Kang, S.H., Raney, J.R., Wang, P., Fang, L., Candido, F., Lewis, J.A., Bertoldi, K.: Multistable architected materials for trapping elastic strain energy. Adv. Mater. **27**(29), 4296–4301 (2015). https://doi.org/10.1002/adma.201501708
5. Liao, X., Chen, L., Zhou, S., Zhang, M.: A novel vari-potential bistable nonlinear energy sink for improved vibration suppression: numerical and experimental study. Nonlinear Dyn. **111**(21), 19763–19790 (2023)
6. Yan, B., Yu, N., Ma, H., Wu, C.: A theory for bistable vibration isolators. Mech. Syst. Signal Process **167**, 108507 (2022). https://doi.org/10.1016/j.ymssp.2021.108507
7. Yang, K., Harne, R.L., Wang, K.W., Huang, H.: Investigation of a bistable dual-stage vibration isolator under harmonic excitation. Smart Mater. Struct. **23**(4), 045033 (2014). https://doi.org/10.1088/0964-1726/23/4/045033
8. Rezaei, M., Talebitooti, R., Liao, W.-H.: Exploiting bi-stable magneto-piezoelastic absorber for simultaneous energy harvesting and vibration mitigation. Int. J. Mech. Sci. **207**, 106618 (2021). https://doi.org/10.1016/j.ijmecsci.2021.106618
9. Noh, J., Kim, P., Yoon, Y.-J.: Competitive advantages of a bistable vibration isolator: cut-off frequency and operational safety near harmful resonance. J. Sound Vib. **570**, 118004 (2024). https://doi.org/10.1016/j.jsv.2023.118004
10. Pellegrini, S.P., Tolou, N., Schenk, M., Herder, J.L.: Bistable vibration energy harvesters: a review. J. Intell. Mater. Syst. Struct. **24**(11), 1303–1312 (2013). https://doi.org/10.1177/1045389X12444940
11. Daqaq, M.F., Masana, R., Erturk, A., Dane Quinn, D.: On the role of nonlinearities in vibratory energy harvesting: a critical review and discussion. Appl. Mech. Rev. **66**(4), 040801 (2014). https://doi.org/10.1115/1.4026278
12. Harne, R.L., Wang, K.W.: A review of the recent research on vibration energy harvesting via bistable systems. Smart Mater. Struct. **22**(2), 023001 (2013). https://doi.org/10.1088/0964-1726/22/2/023001
13. Erturk, A., Hoffmann, J., Inman, D.J.: A piezomagnetoelastic structure for broadband vibration energy harvesting. Appl. Phys. Lett. **94**(25), 254102 (2009). https://doi.org/10.1063/1.3159815
14. Hopf, F., Kaplan, D., Gibbs, H., Shoemaker, R.: Bifurcations to chaos in optical bistability. Phys. Rev. A **25**(4), 2172 (1982)
15. Lorenz, E.: The butterfly effect. World Sci. Ser. Nonlinear Sci. Ser. A **39**, 91–94 (2000)
16. La Roca, L.R., Peterson, J., Cruz Pereira, M., Cunha Jr, A.: Control of chaos via ogy method on a bistable energy harvester. In: 25th ABCM International Congress on Mechanical Engineering (COBEM 2019) (2019)
17. Ott, E., Grebogi, C., Yorke, J.A.: Controlling chaos. Phys. Rev. Lett. **64**(11), 1196 (1990)
18. Fang, X., Lacarbonara, W., Cheng, L.: Advances in nonlinear acoustic/elastic metamaterials and metastructures. Nonlinear Dyn. 1–28 (2024)
19. Intrigila, C., Micheletti, A., Nodargi, N.A., Artioli, E., Bisegna, P.: Fabrication and experimental characterisation of a bistable tensegrity-like unit for lattice metamaterials. Addit. Manuf. **57**, 102946 (2022). https://doi.org/10.1016/j.addma.2022.102946
20. Liu, Y., Pan, F., Xiong, F., Wei, Y., Ruan, Y., Ding, B., Yang, K., Chen, Y.: Ultrafast shape-reconfigurable chiral mechanical metamaterial based on prestressed bistable shells. Adv. Func. Mater. **33**(25), 2300433 (2023). https://doi.org/10.1002/adfm.202300433
21. Liu, Y., Pan, F., Ding, B., Zhu, Y., Yang, K., Chen, Y.: Multistable shape-reconfigurable metawire in 3D space. Extreme Mech. Lett. **50**, 101535 (2022). https://doi.org/10.1016/j.eml.2021.101535
22. Rafsanjani, A., Pasini, D.: Bistable auxetic mechanical metamaterials inspired by ancient geometric motifs. Extreme Mech. Lett. **9**, 291–296 (2016). https://doi.org/10.1016/j.eml.2016.09.001

23. Kamrava, S., Mousanezhad, D., Ebrahimi, H., Ghosh, R., Vaziri, A.: Origami-based cellular metamaterial with auxetic, bistable, and self-locking properties. Sci. Rep. **7**(1), 46046 (2017). https://doi.org/10.1038/srep46046
24. Meng, Z., Chen, W., Mei, T., Lai, Y., Li, Y., Chen, C.Q.: Bistability-based foldable origami mechanical logic gates. Extreme Mech. Lett. **43**, 101180 (2021). https://doi.org/10.1016/j.eml.2021.101180
25. Liu, T., Hao, G.: Design of deployable structures by using bistable compliant mechanisms. Micromachines **13**(5), 651 (2022). https://doi.org/10.3390/mi13050651
26. Zirbel, S.A., Tolman, K.A., Trease, B.P., Howell, L.L.: Bistable mechanisms for space applications. PLoS ONE **11**(12), 0168218 (2016)
27. Wang, B., Zhu, J., Zhong, S., Liang, W., Guan, C.: Space deployable mechanics: a review of structures and smart driving. Mater. Des. **237**, 112557 (2023)
28. Habib, G., Romeo, F.: The tuned bistable nonlinear energy sink. Nonlinear Dyn. **89**(1), 179–196 (2017)
29. Zeng, Y.-C., Ding, H., Du, R.-H., Chen, L.-Q.: Micro-amplitude vibration suppression of a bistable nonlinear energy sink constructed by a buckling beam. Nonlinear Dyn. **108**(4), 3185–3207 (2022)
30. Nadkarni, N., Daraio, C., Kochmann, D.M.: Dynamics of periodic mechanical structures containing bistable elastic elements: from elastic to solitary wave propagation. Phys. Rev. E **90**(2), 023204 (2014). https://doi.org/10.1103/PhysRevE.90.023204
31. Wu, K., Hu, H., Wang, L.: Nonlinear elastic waves in a chain type of metastructure: theoretical analysis and parametric optimization. Nonlinear Dyn. **111**(13), 11729–11751 (2023)
32. Guner, T., Bursi, O.S., Broccardo, M.: Seismic vibration mitigation of steel storage tanks by metafoundations endowed with linear and bistable columns. Bull. Earthq. Eng. **22**(1), 29–54 (2024). https://doi.org/10.1007/s10518-023-01692-0
33. Askari, M., Hutchins, D.A., Thomas, P.J., Astolfi, L., Watson, R.L., Abdi, M., Ricci, M., Laureti, S., Nie, L., Freear, S., Wildman, R., Tuck, C., Clarke, M., Woods, E., Clare, A.T.: Additive manufacturing of metamaterials: a review. Addit. Manuf. **36**, 101562 (2020). https://doi.org/10.1016/j.addma.2020.101562
34. Fan, J., Zhang, L., Wei, S., Zhang, Z., Choi, S.-K., Song, B., Shi, Y.: A review of additive manufacturing of metamaterials and developing trends. Mater. Today **50**, 303–328 (2021). https://doi.org/10.1016/j.mattod.2021.04.019
35. Yang, H., Ma, L.: Multi-stable mechanical metamaterials by elastic buckling instability. J. Mater. Sci. **54**(4), 3509–3526 (2019). https://doi.org/10.1007/s10853-018-3065-y
36. Jeong, H.Y., An, S.-C., Lim, Y., Jeong, M.J., Kim, N., Jun, Y.C.: 3D and 4D printing of multistable structures. Appl. Sci. **10**(20), 7254 (2020). https://doi.org/10.3390/app10207254
37. Meng, Z., Qin, W., Mei, T., Qing Chen, C.: Bi-material sinusoidal beam-based temperature responsive multistable metamaterials. Int. J. Solids Struct. **277–278**, 112343 (2023). https://doi.org/10.1016/j.ijsolstr.2023.112343
38. Chuang, K.-C., Wang, D.-F., Fang, X., Wang, Y.-H., Huang, Z.-L.: Applying bandgap defect modes to crack detection in beams using periodic concentrated masses. J. Sound Vib. **477**, 115308 (2020)
39. Aloschi, F., Bursi, O.S., Palermo, A., Marzani, A.: A time domain procedure for the identification of periodic structures. Int. J. Mech. Sci. **269**, 109054 (2024)
40. Franco, G., Betti, R., Longman, R.W.: On the uniqueness of solutions for the identification of linear structural systems. J. Appl. Mech. **73**(1), 153–162 (2005). https://doi.org/10.1115/1.2062829
41. Thomsen, J.: Vibration and Stability. Springer, Berlin (2003)
42. Rosenstein, M.T., Collins, J.J., De Luca, C.J.: A practical method for calculating largest Lyapunov exponents from small data sets. Physica D **65**(1), 117–134 (1993). https://doi.org/10.1016/0167-2789(93)90009-P
43. COMSOL AB: COMSOL Multiphysics® v. 6.2. COMSOL AB, Stockholm, Sweden (2024). COMSOL AB. Available from: https://www.comsol.com
44. Laboratory, T.A.R.: AprilTag — april.eecs.umich.edu. https://april.eecs.umich.edu/software/apriltag. Accessed 22 May 2024 (2024)
45. Jianbo Shi, Tomasi: Good features to track. In: Proceedings of IEEE Conference on Computer Vision and Pattern Recognition CVPR-94, pp. 593–600. IEEE Comput. Soc. Press, Seattle, WA, USA (1994). https://doi.org/10.1109/CVPR.1994.323794. http://ieeexplore.ieee.org/document/323794/. Accessed 29 Mar 2024
46. Lucas, B.D., Kanade, T.: An iterative image registration technique with an application to stereo vision. In: IJCAI'81: 7th International Joint Conference on Artificial Intelligence, vol. 2. Vancouver, pp. 674–679 (1981). https://hal.science/hal-03697340 Accessed 29 Mar 2024
47. Specker, T., Buchholz, M., Dietmayer, K.: A new approach of dynamic friction modelling for simulation and observation. IFAC Proc. **47**(3), 4523–4528 (2014). https://doi.org/10.3182/20140824-6-ZA-1003.01711